

# A GLOBALLY CONVERGENT METHOD FOR FINDING THE NUMBER OF INTRINSIC MODES ON NARROW-BANDED SIGNALS\*

CHENJIE ZHONG<sup>†</sup>, ZHIPENG LI<sup>†,\*</sup>, SHANGZHI XU<sup>†</sup>  
XIAOHU LI<sup>‡</sup>, LUODAN ZHANG<sup>‡</sup>, AND JIANJUN YUAN<sup>†</sup>

**Abstract.** Automatically determining the number of intrinsic mode functions (IMFs) and their center frequencies in Variational Mode Decomposition (VMD) still remains an open mathematical challenge, which often relies on heuristic prior settings, trial-and-error strategies or complex-field based methods that lack of theoretical guarantees on the convergence. In this article, we proposed a novel variational method based on real field, focusing on evaluating the supporting baseline of a signal's spectrum, to further retrieve the intrinsic mode functions. Our method treats automatic extraction of modes as a constrained optimization problem that adversarially maximizes the baseline integral while penalizing its curvature, and transform the problem into iteratively solving a fourth-order boundary value problem via Lagrangian duality. Furthermore, we establish the rigorous mathematical proof on the global convergence to our algorithm based on dual ascent in function space. Comprehensive numerical experiments on artificial and real-world signals including electrocardiogram (ECG) data show that our method can provide accurate estimates of IMFs and center frequencies, and comparison with methods like Successive VMD also shows our advantages in avoiding redundant modes while ensuring the recovery of necessary components, indicating that we have provided a robust, theoretically grounded initialization routine for VMD.

**Key words.** narrow-banded signals; variational optimization; Intrinsic Mode Function

**MSC codes.** 65K10, 65L10, 68U01, 46N10, 34B05

---

<sup>†</sup>State Key Laboratory of High-speed Maglev Transportation Technology, and Department of Information and Communication Engineering, Tongji University, Shanghai 201804, China

<sup>‡</sup>NingBo Communication Construction Engineering Testing Center Co. Ltd

\*Corresponding author: lizhipeng@tongji.edu.cn

\*Chenjie Zhong and ZhipengLi are co-first authors who contributed equally to this article.

**Funding:** This study is supported by the National Natural Science Foundation of China under Grant No. 61773290 and the Fundamental Research Funds for the Central Universities (22120230311).

**1 Introduction** Variational Mode Decomposition (VMD) decomposes original signals into multiple Intrinsic Mode Functions (IMF) with limited bandwidth with the help of variational optimization.[5] The core of VMD is to minimize the sum of the bandwidths with respect to the estimated IMFs as well as to ensure the sum of all the IMFs is equal to the original signal. In VMD, it is assumed the frequency of each mode is almost compact around a center pulsation and the associated analytic signal is computed by means of Hilbert Transform to get the unilateral frequency spectrum. Then each mode's frequency spectrum was shifted into baseband by multiplying a frequency modulation factor with respect to the estimated center frequency, transforming each band-pass mode into low pass, and the bandwidth can be estimated by  $H^1$  Gaussian smoothness. Afterwards, they decompose the original signal into each modes by minimizing the sum of the bandwidth of each mode with the constraints that the summation of all modes is the original signal. In short, their key variation optimization can be listed as following:

$$(1.1) \quad \min_{u_k, \omega_k} \left\{ \sum_k \left\| \partial_t \left[ \left( \delta(t) + \frac{j}{\pi t} \right) * u_k(t) \right] e^{-j\omega_k t} \right\|_2^2 \right\}$$

$$(1.2) \quad \text{s.t.} \quad \sum_k u_k = f$$

so that each mode can be altered into an associated analytical signal by using Hilbert Transform and shifted into base-band for the following estimation of bandwidth using  $H^1$  Gaussian smoothness with the shifted demodulated components. To solve the problem, one can construct an augmented Lagrangian Function by introducing both quadratic penalty and Lagrangian Multipliers as follows:

$$(1.3) \quad \begin{aligned} \mathcal{L}(u_k, \omega_k, \lambda) = & \alpha \sum_k \left\| \partial_t \left[ \left( \delta(t) + \frac{j}{\pi t} \right) * u_k(t) \right] e^{-j\omega_k t} \right\|_2^2 \\ & + \left\| f - \sum_k u_k \right\|_2^2 + \left\| \lambda, f - \sum_k u_k \right\|_2^2 \end{aligned}$$

This problem can be solved by using ADMM(Alternate Direction Method of Multipliers), in which each component can be updated by solving the equivalent minimization problem:

$$(1.4) \quad u_k^{n+1} = \arg \min_{u_k \in \mathbb{R}} \left\{ \alpha \left\| \partial_t \left[ \left( \delta(t) + \frac{j}{\pi t} \right) * u_k(t) \right] e^{-j\omega_k t} \right\|_2^2 + \left\| f - \sum_i u_i + \frac{\lambda}{2} \right\|_2^2 \right\}.$$

One can rewrite it in frequency domain form, so that convolution becomes multiplication for the convenience of the calculation in subsequent variational operations:

$$(1.5) \quad \hat{u}_k^{n+1} = \arg \min_{\hat{u}_k, \hat{u}_k = \hat{u}_k^T} \left\{ \alpha \|j\omega [1 + \text{sgn}(\omega + \omega_k)] \hat{u}_k(\omega + \omega_k)\|_2^2 + \left\| \hat{f} - \sum_i \hat{u}_i + \frac{\lambda}{2} \right\|_2^2 \right\}.$$

and by substitution of  $\omega \rightarrow \omega + \omega_k$  to perform a translation and considering the Hermitian symmetry of spectrum with respect to the real signals, both terms can be

transformed into half-space integrals with non-negative frequencies:

(1.6)

$$\hat{u}_k^{n+1} = \arg \min_{u_k, \hat{u}_k = \hat{u}_k^T} \left\{ \int_0^\infty 4\alpha(\omega - \omega_k)^2 |\hat{u}_k(\omega)|^2 d\omega + 2 \int \left( \hat{f} - \sum \hat{u}_i + \frac{\hat{\lambda}}{2} \right)^2 d\omega \right\}$$

which can be evaluated by vanishing the first ordered variation of positive frequencies for both signal components and center frequencies

$$(1.7) \quad \hat{u}_k^{n+1} = \left( \hat{f} - \sum_{i \neq k} \hat{u}_i + \frac{\hat{\lambda}}{2} \right) \frac{1}{1 + 2\alpha(\omega - \omega_k)^2}$$

$$(1.8) \quad \omega_k^{n+1} = \frac{\int_0^\infty \omega |\hat{u}_k(\omega)|^2 d\omega}{\int_0^\infty |\hat{u}_k(\omega)|^2 d\omega}$$

Since its establishment, VMD is always playing an important role in modern signal decomposition in many fields[14, 21, 9, 7, 16, 15, 1]. Although VMD has provided flexibility in decomposing signals, there are factors that hinder its further applications in that the number of intrinsic mode function must be determined manually as a prior in coordination with penalty factor without a common principle[19, 10, 18, 17]. In order to alleviate the problem, the subsequent research either needs the knowledge to the range of the number of modes , [11] retrieves the IMFs recursively , [12] or highly dependent on a predefined window-size to retrieve the peak and valley of spectra [6]. All these methods either require prior or rely on schemes devoid of convergence guarantees, making the results contains spurious or missed modes. The absence of a well-posed, convergent paradigm for automatically finding the number of IMFs is a crucial factor that hinders the development of VMD.

To close this gap, we introduce a fundamentally different approach for finding the IMFs. Instead of retrieving modes in an trial-and-error way or recursively extracting modes, we focus on the spectrum amplitude and reformulate the problem by introducing supporting baseline, a lower-enveloping curve of a signal's spectrum which can support the spectrum as tightly as possible while keeping itself as smooth as possible, and transform the problem for finding IMFs into first evaluating the supporting baseline by adversarially maximizing its integral while penalizing its curvature, then retrieving the separated peaks of the original spectrum above the supporting baseline.

Our main contribution can be summarized as 4 folds. First, we give a new perspective for determining the number of IMFs by introducing supporting baseline of spectrum and solve the problem in real field. Second, we derive its optimality conditions, establishing a rigorous equivalence between this variational problem and a fourth-order boundary value problem, and establish rigorous mathematical proof for the global convergence to the course of dual ascent iteration in function space. Thirdly, we develop an efficient iteration scheme for the algorithm by converting the corresponding difference equation and boundary conditions into matrix format and expanding compatible rule to the component-wise multiplication between matrices and vectors for Hadamard product. Finally, we give experiments on both artificial and real signals, and comparison with SVMD to show the robustness of our algorithm and experiments show that our method can quickly get accurate estimation about

the number of IMFs and the corresponding initial center frequencies as prior to the following VMD procedure.

This article will be organized as follows: In the following section we propose the main framework of our algorithm and give the proof of the convergence. In section 3 we introduce the implementation detail about the whole workflow. In Section 4 we design a series of experiments to evaluate the performance of our algorithm. In the final section we show our conclusion about the main contribution of the paper.

**2 Methodology and Convergence Proof** In this section we introduce our method for estimating the number of IMF modes as well as center frequencies of each band. We first introduce the background of the problem, and then we propose the concept of Supporting Baseline of a Function, finally we describe our method for finding the baseline and give the convergence proof for our method.

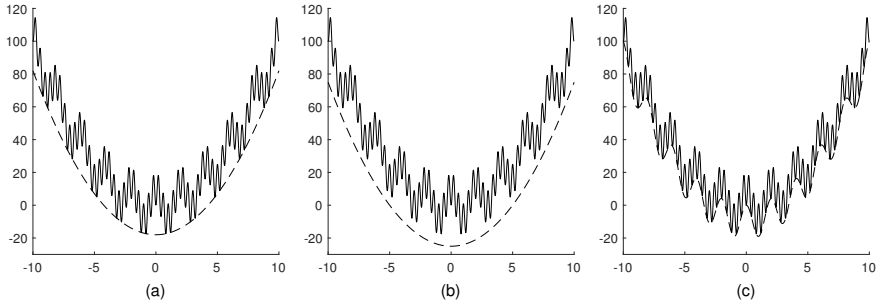


Fig. 1: Illustration to the concept of supporting baseline: In (a)-(c) the solid line is  $y = 10 \cos \pi x - 10 \cos 5\pi x + x^2$ . The dashed line in (a) is a proper supporting baseline since it actually fits the lower bound of the solid line as well as ignoring high frequent details of the solid line. The dashed line in (b) has a gap to the bottom of the solid line so it is not suitable to be a good supporting baseline. In contrast, the dashed line in (c) fits too tightly to the lower bound of the solid line, capturing too much detail of the solid line so that it can be reckoned as the lower envelope rather than a proper supporting baseline.

**2.1 Supporting Baseline of a Function** Without loss of generality we first introduce the Supporting Baseline of a function. For any function  $f(x) > 0$ , the supporting baseline is a curve that tightly fits the lower bound of the function while reflects the overall trend of the lower bound. Fig. 1 gives an intuitive illustration about the conception of supporting baseline. As illustrated in Fig. 1, intuitively the supporting baseline should be tightly close to the lower bound of the function, approaching the infimum of functions as close as possible as well as maintain its own smoothness in order to capture the global trend of the lower bound rather than too much details, as capturing too much details will in turn reduce the robustness for separating the modes since there might be some noise added to the signal in either time or frequency domain.

**2.2 Variational Methods for Finding the Supporting Baseline** To solve the problem for finding the supporting baseline, we use optimization method mainly

based on variation and convex optimization[8, 4]. Let  $f(x) \geq 0$  be a known function, the problem of finding the supporting baseline curve of  $f(x)$  is equivalent to finding a function  $g(x)$  that tightly approaching the point-wise infimum of  $f(x)$  while maintaining the global trend of its lower bound. This can be viewed as the following optimization problem:

$$(2.1) \quad \begin{cases} \max_{g(x)} \int_{\Omega} g(x) dx \\ \min_{g(x)} \int_{\Omega} g''^2(x) dx \end{cases} \text{ w.r.t } \begin{cases} g(x) \leq f(x) \\ g(x) \geq 0 \end{cases}$$

Converting (2.1) into standard form, we get:

$$(2.2) \quad \begin{cases} \min_{g(x)} \int_{\Omega} -g(x) dx \\ \min_{g(x)} \int_{\Omega} g''^2(x) dx \end{cases} \text{ w.r.t } \begin{cases} g(x) - f(x) \leq 0 \\ -g(x) \leq 0 \end{cases}$$

This is an optimization problem with inequality constraints. To solve the problem, one can construct an Lagrange Slack Function by adding functional-styled weights to each factor and constraints

$$(2.3) \quad \begin{aligned} L(g, \lambda, \mu, \alpha, \beta) = & \int_{\Omega} \alpha(x) g''^2(x) dx + \int_{\Omega} \beta(x) [-g(x)] dx \\ & + \int_{\Omega} \lambda(x) [g(x) - f(x)] dx + \int_{\Omega} \mu(x) [-g(x)] dx \end{aligned}$$

where

$$(2.4) \quad \begin{cases} \lambda(x) = 0, f(x) \geq g(x), \forall x \\ \lambda(x) > 0, g(x) > f(x), \forall x \end{cases}$$

$$(2.5) \quad \begin{cases} \mu(x) = 0, g(x) \geq 0, \forall x \\ \mu(x) > 0, g(x) < 0, \forall x \end{cases}$$

and  $\alpha(x), \beta(x) > 0$ . The solution of the problem can be found by solving a variation problem, namely, if we set

$$(2.6) \quad F = \alpha(x) g''^2(x) - \beta(x) g(x) + \lambda(x) [g(x) - f(x)] - \mu(x) g(x)$$

then the above Lagrange Slack Function is like the form  $J[g(x)] = \int_{\Omega} F(x, g, g'') dx$  so that if we assume the variation is zero at both ends of the curve, one can easily know the optimal solution of the above function happen to satisfy the simplified form of Euler-Poisson equation if we let the variation vanish,[8] so it can be written as

$$(2.7) \quad F_g + \frac{d^2 F_{g''}}{dx^2} = 0$$

where

$$(2.8) \quad F_g = -\beta(x) + \lambda(x) - \mu(x)$$

$$(2.9) \quad F_{g''} = 2\alpha(x)g''(x)$$

It is easily to get that

$$(2.10) \quad \frac{d^2 F_{g''}}{dx^2} = 2\alpha''(x)g''(x) + 4\alpha'(x)g^{(3)}(x) + 2\alpha(x)g^{(4)}(x)$$

By substituting (2.8) and (2.10) into (2.7), we can get the following ordinary differential equation

$$(2.11) \quad 2\alpha''(x)g''(x) + 4\alpha'(x)g^{(3)}(x) + 2\alpha(x)g^{(4)}(x) = \beta(x) - \lambda(x) + \mu(x)$$

This is a 4th-ordered Ordinary Differential Equation (ODE), so that normally four constraints are needed to determine a definite solution. Recall that we assume the variation is zero at both ends of the curve, so that we can typically set four constraints at both ends of the curve with respect to the function value and its first-order derivative as follows:

$$(2.12) \quad g(0) = f(0), g(n) = f(n), g'(0) = f'(0), g'(n) = f'(n)$$

where 0 stands for the left end and  $n$  the right end of the curve. To solve the boundary value problem of ODE, we use Finite Difference Method.[20] Note that for a differential function  $g(x)$ , it's derivative of first to fourth order can be expressed as the linear combination of  $g(x)$  itself in the corresponding differential format and we can take similar operation to the function  $\alpha(x)$  (See Supplementary Materials A), so that different orders of derivative with respect to  $\alpha(x)$  and  $g(x)$  can be expressed as the linear combination of themselves, one can easily transform (2.11) into the matrix-form as follows:

$$(2.13) \quad (2\mathbf{A}^{(2)}\boldsymbol{\alpha}) \odot (\mathbf{G}^{(2)}\mathbf{g}) + (4\mathbf{A}^{(1)}\boldsymbol{\alpha}) \odot (\mathbf{G}^{(3)}\mathbf{g}) + (2\boldsymbol{\alpha}) \odot (\mathbf{G}^{(4)}\mathbf{g}) = \boldsymbol{\beta} - \boldsymbol{\lambda} + \boldsymbol{\mu}$$

where  $\mathbf{A}^{(n)}$  and  $\mathbf{G}^{(n)}$  is the conversion matrices (See Supplementary Materials A) that transform the  $n^{\text{th}}$  derivatives of  $\alpha(x)$  and  $g(x)$  into linear expression of the corresponding function,  $\odot$  stands for component-wise multiplication between matrices. The conversion matrices  $\mathbf{A}^{(n)}$  and  $\mathbf{G}^{(n)}$  has the same structure.  $\mathbf{g}$ ,  $\boldsymbol{\alpha}$ ,  $\boldsymbol{\beta}$ ,  $\boldsymbol{\lambda}$ ,  $\boldsymbol{\mu}$  are column vectors obtained by respectively discretizing the corresponding functions, in which each element is a uniformly discrete sampled value on the function  $g(x)$ ,  $\alpha(x)$ ,  $\beta(x)$ ,  $\lambda(x)$ ,  $\mu(x)$ , respectively. The boundary condition is handled at the last 4 line in  $(2\mathbf{A}^{(2)}\boldsymbol{\alpha}) \odot \mathbf{G}^{(2)} + (4\mathbf{A}^{(1)}\boldsymbol{\alpha}) \odot \mathbf{G}^{(3)} + 2\boldsymbol{\alpha} \odot \mathbf{G}^{(4)}$  (See Supplementary A for details). Algorithm 2.1 shows the details of our key steps for evaluating the supporting baseline.

---

**Algorithm 2.1** The Key Steps for Evaluating Support Baseline
 

---

```

1: Input  $\{f(x)\}$ 
2: Initialize  $\alpha(x), \beta(x), \lambda(x), \mu(x), g(x)$ 
3: Pre-process by extending  $f(x)$  at both ends.
4: repeat
5:    $n \leftarrow n + 1$ 
6:   Update  $g(x)$ :
7:     Solve the equation:
8:      $(2\mathbf{A}^{(2)}\alpha) \odot (\mathbf{G}^{(2)}g) + (4\mathbf{A}^{(1)}\alpha) \odot (\mathbf{G}^{(3)}g) + (2\alpha) \odot (\mathbf{G}^{(4)}g) = \beta - \lambda + \mu$ 
9:   Dual ascent:
10:     $\lambda^{n+1} \leftarrow \max\{0, \lambda^n + \theta(g - f)\}$ 
11:     $\mu^{n+1} \leftarrow \max\{0, \mu^n + \gamma(-g)\}$ 
12: until convergence:  $\|g^n - g^{n-1}\|_2^2 / \|g^n\|_2^2 < \epsilon$ 
  
```

---

**2.3 Proof of the Convergence** One of the core contribution of this work is to provide a deterministic, global convergence guarantees for the problem of automatic mode detection, which is typically unaddressed in the pioneer works. we prove that the algorithm generates sequences converging to an optimal solution of the original problem. The proof is built upon several folds:

**Convexity and Duality:** Proof of the problem's convexity and strong duality.

**Well-posedness of Iterations:** Demonstration that each iterative step solves a well-posed subproblem with a unique solution.

**Convergence in Dual Space:** Impose functional functional to dual ascent method and analyse its convergence under both unique and non-unique optimal dual solutions.

**Convergence in Primal Space:** Establish the convergence of the primal sequence via the continuous dependence of solutions on parameters.

For the conciseness of the proof, we leave the detail of the the convexity and duality into Appendix and focus on the well-posedness of iterations and convergence in dual and primal spaces here.

**2.3.1 Convexity and Duality** In this part we state the main results about the convexity and duality, and we put the details in Appendix B.1 and B.2.

LEMMA 2.1. *The objection functional of (2.2) is convex, and the feasible set is also convex.*

LEMMA 2.2. *The dual of objection functional of (2.2) is concave, with the dual-gap zero.*

**2.3.2 Well-posedness of Iterations** Before analyzing the convergence of the iterative algorithm, we must ensure that the subproblem solved at each iteration is well-posed. Specifically, as in each iteration, our primal solution  $g_{k+1}(x)$  is given by dual variables  $(\lambda_k(x), \mu_k(x))$  at the  $k$ -th step and we transform the variational problem into a linear fourth-order boundary value problem (BVP), the well-posedness of this BVP encompassing the existence and uniqueness of the solution is crucial to guarantee that our iterative scheme is not only well-defined but also stable against small numerical perturbations. Since  $\alpha(x)$  and  $\beta(x)$  in our algorithm can be considered as weights function that are always positive, we can establish the existence and uniqueness of our solution to (2.11) below.

**THEOREM 2.3.** *Assume  $\alpha(x) > 0$ , then the solution of (2.11) with  $g(0) = 0$ ,  $g(n) = 0$ ,  $g'(0) = 0$ ,  $g'(n) = 0$  is  $g(x) \equiv 0$ .*

*Proof.* Recall that when dealing with the homogeneous condition, we exactly have

$$(2.14) \quad g(x) = \int_a^x \left( \int_a^x \frac{C_1 t + C_2}{\alpha(t)} dt \right) dt + C_3 x + C_4$$

where

$$(2.15) \quad g(a) = g(b) = g'(a) = g'(b) = 0$$

It is obvious that  $C_3$  and  $C_4$  are zero by  $g(a)$  and  $g'(a)$ , and  $g'(b) = 0$  is equivalent to

$$(2.16) \quad \int_a^b \frac{C_1 t + C_2}{\alpha(t)} dt = 0$$

Since  $\alpha(t) > 0$  and  $\alpha(t) \in C[a, b]$ , since  $C_1 t + C_2$  is a linear function so that if the zero point is not in  $[a, b]$  then it is not possible to make (2.16) hold. If there exists  $t \in [a, b]$  that makes  $C_1 t + C_2$  zero, then the upper limit integral function  $\Phi(x) = \int_a^x \frac{C_1 t + C_2}{\alpha(t)} dt$  has no zero points in  $(a, b)$ , thus makes  $g(b) = \int_a^b \Phi(t) dt$  non-zero, which is paradoxical to our assumption if not both  $C_1$  and  $C_2$  are zero. Then according to Fredholm Alternative Theorem, we can assert that during each iteration, there always exist a unique solution to  $g(x)$  [26, 27, 28].  $\square$

**COROLLARY 2.4.** *For each iteration of (2.13), there always exists a unique solution.*

**2.3.3 Convergence in Dual Space** To facilitate the convergence analysis in the dual space, we introduce the following regularity assumptions on the primal problem:

The target spectrum function  $f(x)$  is Lipschitz continuous on  $\mathcal{D}$ .

The solution  $g(x)$  to the subproblem and the iterates  $g_k(x)$  reside in  $C^2(\mathcal{D})$  with uniformly bounded second derivatives.

These assumptions are standard for analyzing variational problems involving curvature penalties. In practice, for discrete and potentially noisy spectral data,  $f(x)$  can be considered as a smooth interpolation of the observed points. Crucially, the core object of interest—the supporting baseline—is intrinsically a smooth function due to the curvature penalty term in the objective. Therefore, the analysis under these smoothness assumptions captures the essential behavior of the algorithm.

We begin the proof by first restating the iteration in Algorithm 2.1. Notice that during the iteration, we have

$$(2.17) \quad \begin{cases} g_{k+1}(x) = \arg \min_{g(x)} \mathcal{L}(g(x), \lambda_k(x), \mu_k(x)) \\ \lambda_{k+1}(x) = \max[0, \lambda_k(x) + \theta(g_{k+1}(x) - f(x))] \\ \mu_{k+1}(x) = \max[0, \mu_k(x) + \gamma(-g_{k+1}(x))] \end{cases}$$

To show the projection property for the max operation we first prove the following lemma:

LEMMA 2.5. Let  $m(x), x \in \mathcal{D}$  be any continuous function that has both positive and negative values, Let  $\Pi$  be an operator that makes all the negative values for  $m(x)$  zero and non-negative unchanged, or  $\Pi m(x) = \max(0, m(x))$ , let  $M(x), x \in \mathcal{D}$  be any non-negative function, then

$$(2.18) \quad \int_{\mathcal{D}} [m(x) - \Pi m(x)] [M(x) - \Pi m(x)] dx \leq 0$$

*Proof.* By expanding the equation (2.18) we should have the following:

$$(2.19) \quad \begin{aligned} & \int_{\mathcal{D}} [m(x) - \Pi m(x)] [M(x) - \Pi m(x)] dx \\ &= \int_{\mathcal{D}} m(x)M(x)dx - \int_{\mathcal{D}} \Pi m(x)M(x)dx - \int_{\mathcal{D}} m(x)\Pi m(x)dx + \int_{\mathcal{D}} [\Pi m(x)]^2 dx \\ &= \int_{\mathcal{D}} m(x)M(x)dx - \int_{\mathcal{D}} \Pi m(x)M(x)dx - \int_{\mathcal{D}} [\Pi m(x)]^2 dx + \int_{\mathcal{D}} [\Pi m(x)]^2 dx \\ &\leq \int_{\mathcal{D}} m(x)M(x)dx - \int_{\mathcal{D}} m(x)M(x)dx - \int_{\mathcal{D}} [\Pi m(x)]^2 dx + \int_{\mathcal{D}} [\Pi m(x)]^2 dx = 0 \end{aligned}$$

Moreover, if  $m(x)$  is in feasible set so that  $m(x) = \Pi m(x)$ , then (2.19) will become zero.  $\square$

Now we prove that in iteration (2.17) the multiplier  $\lambda_k(x), \mu_k(x)$  always terminate at one of the optimum. To say in detail, we should have the following theorem:

THEOREM 2.6. Let  $\mathcal{G}(\lambda(x), \mu(x)) = \arg \min_{g(x)} \mathcal{L}(g(x), \lambda(x), \mu(x))$  and  $\lambda_k(x), \mu_k(x)$  be equicontinuous for all  $k = 1, 2, 3, \dots$ , then if  $\mathcal{G}$  satisfies

$$(2.20) \quad \begin{aligned} & ||D[\mathcal{G}(\lambda_1(x), \mu_1(x)) - \mathcal{G}(\lambda_2(x), \mu_2(x))]]|| \\ & \leq L ||[\lambda_1(x) - \lambda_2(x), \mu_1(x) - \mu_2(x)]|| \end{aligned}$$

for any  $\lambda_1(x), \lambda_2(x), \mu_1(x), \mu_2(x)$ , where  $D$  stands for the variation, and the step size  $\eta < \frac{1}{L}$ , then as  $k \rightarrow +\infty$ , the iteration series of  $(\lambda_k(x), \mu_k(x))$  must terminate at the point as close as possible to one of the optimum  $(\lambda^*(x), \mu^*(x))$  for  $\mathcal{G}$ .

*Proof.* For conciseness, simplifying the integral by introducing matrix-form expression, where

$$(2.21) \quad \begin{bmatrix} a(x) & b(x) \end{bmatrix} \begin{bmatrix} c(x) \\ d(x) \end{bmatrix} = \int_{\mathcal{D}} a(x)c(x)dx + \int_{\mathcal{D}} b(x)d(x)dx$$

we have

$$(2.22) \quad \begin{bmatrix} \tilde{\lambda}_{k+1}(x) - \lambda_{k+1}(x) & \tilde{\mu}_{k+1}(x) - \mu_{k+1}(x) \end{bmatrix} \begin{bmatrix} \lambda_k(x) - \lambda_{k+1}(x) \\ \mu_k(x) - \mu_{k+1}(x) \end{bmatrix} \leq 0$$

by considering all possible locations for  $(\tilde{\lambda}_{k+1}(x), \tilde{\mu}_{k+1}(x))$ , where  $(\tilde{\lambda}, \tilde{\mu})$  stands for general points before assigning the operator  $\Pi$ , or  $\max(0, \cdot)$  compared with  $(\lambda, \mu)$ . Expand (2.22) and rearrange, we have

$$(2.23) \quad D\mathcal{G}_{(\lambda_k(x), \mu_k(x))}(\lambda_k(x), \mu_k(x)) \begin{bmatrix} \lambda_{k+1}(x) - \lambda_k(x) \\ \mu_{k+1}(x) - \mu_k(x) \end{bmatrix} \geq \frac{1}{\eta} \left\| \begin{bmatrix} \lambda_{k+1}(x) - \lambda_k(x) \\ \mu_{k+1}(x) - \mu_k(x) \end{bmatrix} \right\|_2^2$$

On the other side, for any functional we have

$$\begin{aligned}
 \mathcal{G}(\lambda_{k+1}(x), \mu_{k+1}(x)) &= \mathcal{G}(\lambda_k(x), \mu_k(x)) \\
 &+ D\mathcal{G}_{(\lambda_k(x), \mu_k(x))}(\lambda(x), \mu(x))^\top \begin{bmatrix} \lambda_{k+1}(x) - \lambda_k(x) \\ \mu_{k+1}(x) - \mu_k(x) \end{bmatrix} \\
 &+ \frac{1}{2!} [\lambda_{k+1}(x) - \lambda_k(x) \quad \mu_{k+1}(x) - \mu_k(x)] \\
 (2.24) \quad &D^2\mathcal{G}_{(\lambda(x), \mu(x))}(\varepsilon_k(x), \zeta_k(x)) \begin{bmatrix} \lambda_{k+1}(x) - \lambda_k(x) \\ \mu_{k+1}(x) - \mu_k(x) \end{bmatrix}
 \end{aligned}$$

where  $(\varepsilon_k(x), \zeta_k(x))$  locates on general line segment from  $(\lambda_k(x), \mu_k(x))$  to  $(\lambda_{k+1}(x), \mu_{k+1}(x))$ . If  $\mathcal{G}$  is second-order differentiable and satisfies (2.6) so that  $\|D^2\mathcal{G}\|$  is bounded with  $[-L, L]$ . Due to the concavity of  $\mathcal{G}$  and the left side of the bound, and combine (2.23) we get

(2.25)

$$\mathcal{G}(\lambda_{k+1}(x), \mu_{k+1}(x)) - \mathcal{G}(\lambda_k(x), \mu_k(x)) \geq \left( \frac{1}{\eta} - \frac{L}{2} \right) \left\| \begin{bmatrix} \lambda_{k+1}(x) - \lambda_k(x) \\ \mu_{k+1}(x) - \mu_k(x) \end{bmatrix} \right\|_2^2 \geq 0$$

if  $\eta = \max\{\theta, \gamma\} = \frac{1}{L} < \frac{2}{L}$ , then  $\mathcal{G}$  is a monotonously increasing functional series with upper bound due to its concavity, so that  $\mathcal{G}$  converges and the difference between adjacent term of both  $\mathcal{G}$  and  $(\lambda_k(x), \mu_k(x))$  is approaching zero.

Now we prove  $\{g_k(x)\}$  is guaranteed to approach one of the optimum when the algorithm terminates even if  $\mathcal{G}$  is not strongly concave. By introducing  $l(\mathbf{y}; \mathbf{x}) = \mathcal{G}(\mathbf{x}) + D\mathcal{G}(\mathbf{x})(\mathbf{y} - \mathbf{x})$  and due to the concavity the iteration on  $\mathcal{G}$  should satisfy [2]

$$\begin{aligned}
 &l \left( \begin{bmatrix} \lambda_{k+1}(x) \\ \mu_{k+1}(x) \end{bmatrix}; \begin{bmatrix} \lambda_k(x) \\ \mu_k(x) \end{bmatrix} \right) - \frac{1}{2\eta} \left\| \begin{bmatrix} \lambda_{k+1}(x) - \lambda_k(x) \\ \mu_{k+1}(x) - \mu_k(x) \end{bmatrix} \right\|_2^2 \\
 &\geq l \left( \begin{bmatrix} \lambda^*(x) \\ \mu^*(x) \end{bmatrix}; \begin{bmatrix} \lambda_k(x) \\ \mu_k(x) \end{bmatrix} \right) - \frac{1}{2\eta} \left\| \begin{bmatrix} \lambda^*(x) - \lambda_k(x) \\ \mu^*(x) - \mu_k(x) \end{bmatrix} \right\|_2^2 \\
 (2.26) \quad &+ \frac{1}{2\eta} \left\| \begin{bmatrix} \lambda^*(x) - \lambda_{k+1}(x) \\ \mu^*(x) - \mu_{k+1}(x) \end{bmatrix} \right\|_2^2
 \end{aligned}$$

since  $-\mathcal{G}$  is convex. Due to the concavity of  $\mathcal{G}$ , we have

$$(2.27) \quad \mathcal{G}(\lambda_{k+1}(x), \mu_{k+1}(x)) \geq l \left( \begin{bmatrix} \lambda_{k+1}(x) \\ \mu_{k+1}(x) \end{bmatrix}; \begin{bmatrix} \lambda_k(x) \\ \mu_k(x) \end{bmatrix} \right) - \frac{1}{2\eta} \left\| \begin{bmatrix} \lambda_{k+1}(x) - \lambda_k(x) \\ \mu_{k+1}(x) - \mu_k(x) \end{bmatrix} \right\|_2^2$$

and

$$(2.28) \quad l \left( \begin{bmatrix} \lambda^*(x) \\ \mu^*(x) \end{bmatrix}; \begin{bmatrix} \lambda_k(x) \\ \mu_k(x) \end{bmatrix} \right) \geq \mathcal{G}(\lambda^*(x), \mu^*(x))$$

Substituting (2.27) and (2.28) into (2.26), then we have

$$\begin{aligned}
 \left\| \begin{bmatrix} \lambda^*(x) - \lambda_{k+1}(x) \\ \mu^*(x) - \mu_{k+1}(x) \end{bmatrix} \right\|_2^2 &\leq 2\eta[\mathcal{G}(\lambda_{k+1}(x), \mu_{k+1}(x)) \\
 (2.29) \quad &- \mathcal{G}(\lambda^*(x), \mu^*(x))] + \left\| \begin{bmatrix} \lambda^*(x) - \lambda_k(x) \\ \mu^*(x) - \mu_k(x) \end{bmatrix} \right\|_2^2
 \end{aligned}$$

Sum up (2.29) for each  $k$  and eliminate the repeated terms that occur at the both ends of the inequality, we have

$$(2.30) \quad \begin{aligned} \left\| \begin{bmatrix} \lambda^*(x) - \lambda_{k+1}(x) \\ \mu^*(x) - \mu_{k+1}(x) \end{bmatrix} \right\|_2^2 &\leq 2\eta \sum_{i=0}^k [\mathcal{G}(\lambda_{i+1}(x), \mu_{i+1}(x)) \\ &\quad - \mathcal{G}(\lambda^*(x), \mu^*(x))] + \left\| \begin{bmatrix} \lambda^*(x) - \lambda_0(x) \\ \mu^*(x) - \mu_0(x) \end{bmatrix} \right\|_2^2 \end{aligned}$$

As the left side is non-negative, and recall in (2.25) we know that  $\{\mathcal{G}_k\}$  is non-decreasing and  $\mathcal{G}^*$  is the supreme of  $\mathcal{G}$ , hence  $\mathcal{G}(\lambda_{k+1}(x), \mu_{k+1}(x)) - \mathcal{G}(\lambda^*(x), \mu^*(x))$  is the largest among all the terms involved in the summation, by applying reasonable inequality scaling we must have

$$(2.31) \quad 0 \geq \mathcal{G}(\lambda_{k+1}(x), \mu_{k+1}(x)) - \mathcal{G}(\lambda^*(x), \mu^*(x)) \geq -\frac{1}{2\eta(k+1)} \left\| \begin{bmatrix} \lambda^*(x) - \lambda_0(x) \\ \mu^*(x) - \mu_0(x) \end{bmatrix} \right\|_2^2$$

which shows the iteration is approaching the optimum. From (2.29) and by utilizing the monotonicity of the functional  $\mathcal{G}$  during iteration we have

$$(2.32) \quad \left\| \begin{bmatrix} \lambda^*(x) - \lambda_{k+1}(x) \\ \mu^*(x) - \mu_{k+1}(x) \end{bmatrix} \right\|_2^2 \leq \left\| \begin{bmatrix} \lambda^*(x) - \lambda_k(x) \\ \mu^*(x) - \mu_k(x) \end{bmatrix} \right\|_2^2$$

which shows the distance between the iterating points and the optimum is always decreasing, since the distance is always non-negative so that it has lower bound,  $(\lambda_k(x), \mu_k(x)) - (\lambda^*(x), \mu^*(x))$  is a convergent sequence so that  $(\lambda_k(x), \mu_k(x))$  is bounded. According to Arzelà-Ascoli Theorem, we can only assert that there exists some sub-sequences  $(\lambda_{k_i}(x), \mu_{k_i}(x))$  that converges, which does not indicate that the whole iterating sequence is necessarily convergent in all cases and needs careful discussion. There are four cases when the iterating sequence is approaching the optimum:

CASE I: If there is only one optima in  $\mathcal{G}$ , then it is trivial to show that all these sub-sequences converges to the unique optimum by the constraints in (2.31).

CASE II: If the optimum of  $\mathcal{G}$  forms a convex set, and during the iteration the sequence  $(\lambda_k(x), \mu_k(x))$  is approaching and never fall into the optimal set, then from the middle parts of (2.31) and (2.25) we know that the value of  $\mathcal{G}$  is approaching the minima and the distance between adjacent term of the sequence  $(\lambda_k(x), \mu_k(x))$  and  $(\lambda_{k+1}(x), \mu_{k+1}(x))$  is yielding zero. Thus we know in this case the iterating sequence in dual space can always terminate to the point as close as possible to one of the optimum, although the classical convergent behaviour for the sequence in this case might not be guaranteed.

CASE III: If the iterating sequence has approached to the unique optima during some steps, then due to (2.32) the next iteration will still stay at the unique optima.

CASE IV: If the optimum of  $\mathcal{G}$  forms a convex set, and the iterating sequence has approached to one of the optimum  $(\lambda_1^*(x), \mu_1^*(x))$  early during some iterating step, then since in the convex set there are at least another optima  $(\lambda_2^*(x), \mu_2^*(x))$ , then we have

$$(2.33) \quad \begin{aligned} \mathcal{G}(m\lambda_1^*(x) + (1-m)\lambda_2^*(x), m\mu_1^*(x) + (1-m)\mu_2^*(x)) \\ = \mathcal{G}(\lambda_1^*(x), \mu_1^*(x)) = \mathcal{G}(\lambda_2^*(x), \mu_2^*(x)), m \in [0, 1] \end{aligned}$$

since the direction of the line connecting the median point and the initial point in the first-order Taylor expansion formula is consistent with  $\begin{bmatrix} \lambda_2^*(x) - \lambda_1^*(x) \\ \mu_2^*(x) - \mu_1^*(x) \end{bmatrix}$ , so we have

$$(2.34) \quad D\mathcal{G}_{(\lambda_k(x), \mu_k(x))}(\lambda(x), \mu(x)) \begin{bmatrix} \lambda_2^*(x) - \lambda_1^*(x) \\ \mu_2^*(x) - \mu_1^*(x) \end{bmatrix} = 0$$

thus the variation direction is always orthogonal to any lines connected between different optima, as a consequence, when projected again during the next iteration,  $(\lambda_{k+1}(x), \mu_{k+1}(x))$  must overlap with  $(\lambda_k(x), \mu_k(x))$ , so we have  $(\lambda_{k+1}(x), \mu_{k+1}(x)) = (\lambda_k(x), \mu_k(x))$ .

In all cases we show  $(\lambda_k(x), \mu_k(x))$  can always terminate at the point as close as possible to at least one of the optimum and stay still as long as it arrives the optimum during the iteration even if there are more than one optimum in  $\mathcal{G}$ .  $\square$

### 2.3.4 Convergence in Primal Space

**THEOREM 2.7.** *Under the convergence of dual sequence as stated in Theorem 2.6, the primal sequence  $\{g_k(x)\}$  generated by Algorithm 2.1 converges to the optimal solution  $g^*(x)$ , specifically, we have  $\lim_{k \rightarrow +\infty} \|g_k(x) - g^*(x)\| = 0$ .*

*Proof.* As the solution of (2.2) is continuously dependent on its coefficients, so we have  $\lim_{k \rightarrow +\infty} g_k(x) = g^*(x)$  when  $\{(\lambda_k(x), \mu_k(x))\}$  when in Case I, III and IV, and  $g_k(x)$  is approaching  $g^*(x)$  when  $\|g_{k+1}(x) - g_k(x)\|$  is approaching zero in Case II respectively. In all cases we can terminate algorithm and guarantee the  $\{g_k(x)\}$  terminates to one of the optimum as close as possible.  $\square$

**3 Implementation** In this chapter, we focus on the detail about the implementation and numerical scheme about the algorithm for evaluating problem (2.2). Our workflow consists of 4 interconnected stages: (1) We discretize (2.11) by using Finite Difference Method,[20] transforming it into a linear system. (2) Crucially, by expressing the derivations of both solution  $g(x)$  and the weight function  $\alpha(x)$  as linear combination of their nodal values, we recast the entire ODE into a compact matrix form by introducing component-wise multiplication with a mild extension of Hadamard production. By imposing well-posed boundary conditions, we make the coefficient matrices full-rank and the whole problem invertible so that the evaluation can be significantly accelerated by modern software toolkits via matrix operation. (3) To further accelerate the convergence and make algorithm effective when handling high or low-passed signals, a smooth extrapolation technique is applied to the input spectrum at the both ends. (4) Finally, after obtaining the optimal baseline, a statistically grounded threshold determined via kernel density estimation (KDE), is employed to automatically identify significant spectral peaks, thereby completing the mode extraction. The following subsections detail each of these components.

**3.1 Spatial Discretization Scheme** We discretize the solution domain  $\Omega = [a, b]$  into  $N + 1$  equally spaced nodes  $x_0, x_1, \dots, x_n$ , where  $x_0 = a$  and  $x_n = b$ , with the grid spacing  $h = \frac{b-a}{N}$ , thus the value of any continuous function  $p(x)$  at the nodes are recorded as a column vector  $\mathbf{p} = [p(x_0), p(x_1), \dots, p(x_N)]^\top \in \mathbb{R}^{N+1}$ . Then we employ Five-Point Central Difference Scheme to transform different orders of derivatives into the linear combination with respect to the primal nodal values. For instance, for the fourth-order derivative  $g^{(4)}(x)$  at interior nodes  $x_i, i = 2, 3, \dots, N-2$

we have

$$(3.1) \quad g^{(4)}(x_i) \approx \frac{g(x_{i+2}) - 4g(x_{i+1}) + 6g(x_i) - 4g(x_{i-1}) + g(x_{i-2})}{h^4}$$

and the corresponding boundary conditions can be approximately expressed as

$$(3.2) \quad \begin{cases} g(0) = g(x_0) \\ g(n) = g(x_N) \\ g'(0) \approx \frac{g(x_1) - g(x_0)}{h} \\ g'(n) \approx \frac{g(x_N) - g(x_{N-1})}{h} \end{cases}$$

Note that (3.1) and (3.2) can be transformed into compact matrix form via a pentadiagonal matrix  $\mathbf{G}^{(4)} \in \mathbb{R}^{(N+1) \times (N+1)}$ , thus we have

$$(3.3) \quad \mathbf{G}^{(4)} = \begin{bmatrix} 1 & -4 & 6 & -4 & 1 & 0 & \cdots & \cdots & \cdots & 0 \\ 0 & 1 & -4 & 6 & -4 & 1 & 0 & \cdots & \cdots & 0 \\ \vdots & \vdots \\ 0 & \cdots & \cdots & 0 & 1 & -4 & 6 & -4 & 1 & 0 \\ 0 & 0 & \cdots & \cdots & 0 & 1 & -4 & 6 & -4 & 1 \end{bmatrix}$$

thus  $\mathbf{G}^{(4)}\mathbf{g}$  is the fourth-ordered derivative of  $\mathbf{g}$  at each node and the non-zero entry stands for the corresponding coefficients of difference and boundary conditions.  $\mathbf{G}^{(3)}$ ,  $\mathbf{G}^{(2)}$ ,  $\mathbf{G}^{(1)}$  and  $\mathbf{A}^{(4)}$  to  $\mathbf{A}^{(1)}$  have the similar structure as  $\mathbf{G}^{(4)}$ , we give the detail of each pentadiagonal matrix in A.

By integrating both the difference strategy and the boundary condition (2.11) is transformed into (2.13), where  $\odot$  stands for component-wise multiplication. However, in (2.13)  $\mathbf{g}$  is inseparable so that we cannot resort to effective evaluation. To solve this, our  $\odot$  is just an extension of standard Hadamard production by adding some compatible broadcasting rules in dealing with column vector, that is  $\forall \mathbf{A}_{m \times n}, \mathbf{v}_{m \times 1}$ , we have

$$(3.4) \quad \mathbf{v} \odot \mathbf{A} = \mathbf{A} \odot \mathbf{v} = \mathbf{A} * \mathbf{V}_{m \times n}$$

where  $*$  stands for standard Hadamard production and each column of  $\mathbf{V}$  is just a copy of  $\mathbf{v}$ . By applying this rule we have  $(\mathbf{A}\mathbf{a}) \odot (\mathbf{B}\mathbf{b}) = ((\mathbf{A}\mathbf{a}) \odot \mathbf{B})\mathbf{b}$ , we can transform (2.13) into

$$(3.5) \quad ((2\mathbf{A}^{(2)}\boldsymbol{\alpha}) \odot \mathbf{G}^{(2)})\mathbf{g} + ((4\mathbf{A}^{(1)}\boldsymbol{\alpha}) \odot \mathbf{G}^{(3)})\mathbf{g} + ((2\boldsymbol{\alpha}) \odot \mathbf{G}^{(4)})\mathbf{g} = \boldsymbol{\beta} - \boldsymbol{\lambda} + \boldsymbol{\mu}$$

so that we can treat (2.13) as common matrix equation and get the solution by simply using matrix inversion with modern mathematical software toolkits.

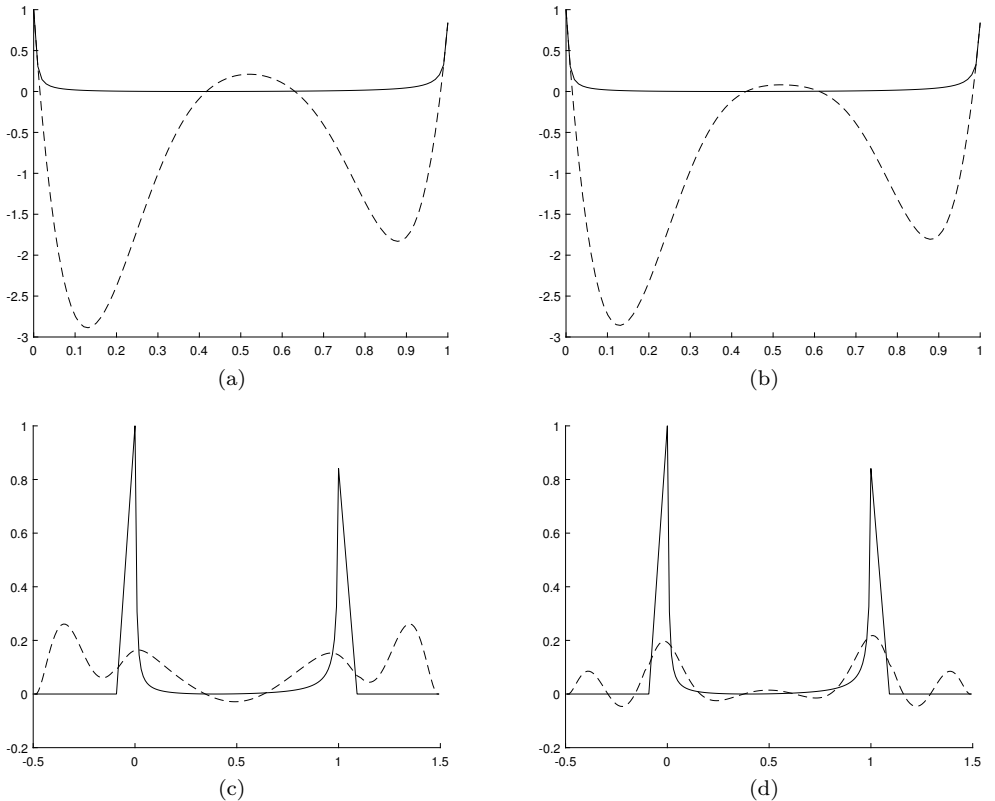


Fig. 2: Iterations for finding the supporting baseline without ((a) and (b)) /with ((c) and (d)) smooth extrapolation to the spectrum when iterated to 500 ((a) and (c)) and 1500 ((b) and (d)) steps for the same spectrum. The solid line is the original spectrum and the dotted line is the evaluated supporting baseline. With smooth extrapolation to the original spectrum, the speed of convergence has significant improvement.

**3.2 Treatment of Boundary Conditions** The primal problem requires the supporting baseline  $g(x)$  confirming with the value of  $f(x)$  and  $f'(x)$  at both ends as boundary conditions, this conducts linear constraints directly onto the first and last elements to the solution vector of  $\mathbf{g}$ . For low and high pass signals of which the spectrum value are high and drop abruptly at either of the ends, this will make  $g(x)$  inherits the trend of  $f(x)$  at both ends at some interval so that convergence in this case will be very slow with reasonable grid space. To alleviate this effect, we adopt a smooth extrapolation strategy by symmetrically appending gently decaying segments at both ends to make the extended value align with the minimum of  $f(x)$ , and the extended derivative smoothly approach to zero within the extended region. This strategy significantly improves the condition number of the coefficient matrix of the discrete system, ensuring the numerical stability of the iterative solution, without any altering the primal spectrum within the original interval. Fig. 2 shows the illustrations.

**3.3 Postprocessing: From Baseline to Mode Identification** Upon the above course when the algorithm converges, we obtain the optimal discrete baseline

vector  $\mathbf{g}^*$  above which significant intrinsic modes corresponds to the parts of the original spectrum  $\mathbf{f}$  that protrude distinctly. However, there are some residual background fluctuations at the bottom that hinders one to objectively distinguish those modes. To solve this problem, we assume that the residual consists of two components: first, a background fluttering component originate from noise or minor undulations, of which the amplitude concentrates within a very small range; second, significant protrusions from original modes, which are larger compared with the former and more scattered. In this view, when investigating the value of the residual spectrum value distribution, we can intuitively find that most values concentrate near the level where fluttering component resides. This inspires us to employ Kernel Density Estimation (KDE) to non-parametrically model the spectrum value distribution as a probability density function:

$$(3.6) \quad \phi(t) = \frac{1}{mh} \sum_{i=1}^m K\left(\frac{t - r_j}{h}\right)$$

where  $K(\cdot)$  is Gaussian function, with  $h$  the bandwidth and  $r_j$  the discrete nodes in the residual vector  $\mathbf{r}$ , and we evaluate the best threshold to eliminate the fluttering noise as

$$(3.7) \quad t^* = \arg \max_t \phi(t)$$

so that we can isolate each mode in the function  $f(x) - g^*(x) - t^*$ .

**3.4 The Whole Workflow** Based on the above discrete framework, each step of Algorithm 2.1 can be implemented by specific linear algebraic operations. The whole workflow can be summarized as Algorithm 3.1. We first input the original spectrum  $f(x)$ , then we initialize weight functions  $\alpha(x), \beta(x)$ , penalty functions  $\lambda(x), \mu(x)$  and the supporting baseline function  $g(x)$ . After that we smoothly extend  $f(x)$  at both ends and begin Algorithm 2.1 until it converges. Then we do Kernel Density Estimation to figure out the threshold to eliminate the fluttering noise, so as to isolate band components.

---

**Algorithm 3.1** The Whole Workflow

---

- 1: Input  $\{f(x)\}$
- 2: Initialize  $\alpha(x), \beta(x), \lambda(x), \mu(x), g(x)$
- 3: Smoothly Extending  $f(x)$  at both ends.
- 4: **repeat**
- 5:   Run the kernel process of Algorithm 2.1
- 6: **until** convergence:  $\|g^n - g^{n-1}\|_2^2 / \|g^n\|_2^2 < \epsilon$
- 7: Estimate KDE for the computed  $g(x)$ .
- 8: Compute best threshold  $t_{best} = \arg \max \text{KDE}_{g(x)}(t)$ .
- 9: Subtract noise-gap threshold from  $g(x)$  by  $g(x) - t_{best}$ .
- 10: Get  $k, \{\omega_k\}$  from non-zero intervals.
- 11: Begin VMD procedure [5] with  $k$  and  $\{\omega_k\}$
- 12: Output  $\{u_k\}$

---

**4 Numerical Results** In this section, we show some experiments to validate the applicability of our methods. Our experiments focus on 3 goals: (1) To validate

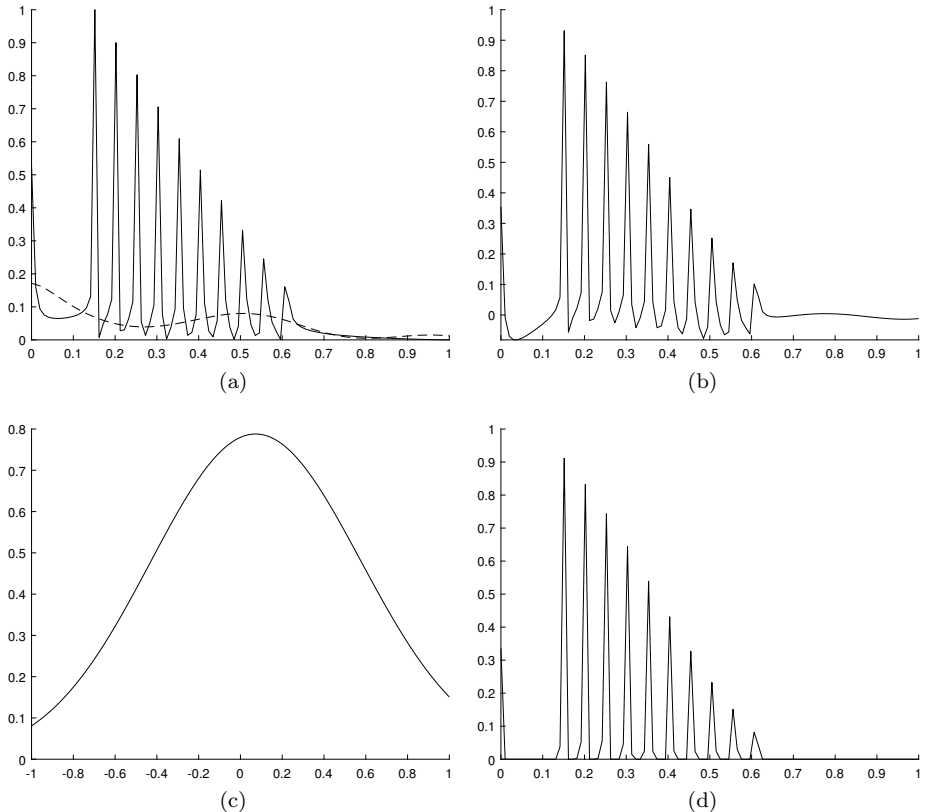


Fig. 3: Illustration of the non-consistence of the error between the converged optimal supporting baseline and the original function. Fig. 3a shows the converged  $g(x)$  and Fig. 3b shows  $f(x) - g(x)$ . Note that since  $g(x)$  does have gap to the lower bound of  $f(x)$  so that the bottom of  $f(x) - g(x)$  is almost not on a horizontal line everywhere, which indicates there are some non-zero gaps. These non-zero gaps will have a significant impact on the stability of the subsequent modal number solution. 3c shows the estimate kernel density pertaining the gap at the bottom. 3d shows the estimated  $f(x) - g(x)$  after removal of the gap at the bottom.

the convergence and robustness of our method under synthetic signals like single-modality signal, dual-modality signal, segmented signal, comb-spectrum signal, dense-modality signal to demonstrate the extensive adaptability of the model across modes with various distribution. (2) To compare our method against the most challengeable method Successive Variational Mode Decomposition (SVMD), another recursive, adaptive method determining the intrinsic modes, exhibiting the advantage of our method on not generating redundant modes or eliminating necessary modes. (3) To understand the applicability of our method in real-world signals like electrocardiogram (ECG) signals, showing the accuracy of decomposition by investigation of the signals reconstructed from the decomposed modes.

All experiments are conducted under the same parameter settings unless other-

wise stated. The stopping criterion is set as  $\frac{\|g_n - g_{n-1}\|}{\|g_n\|} < 10^{-4}$ . The number of discrete grid points is fixed at  $N = 200$  for the normalized frequency domain  $[0, 1]$ . Detailed descriptions of the test signals and comparative protocols are provided in the corresponding subsections.

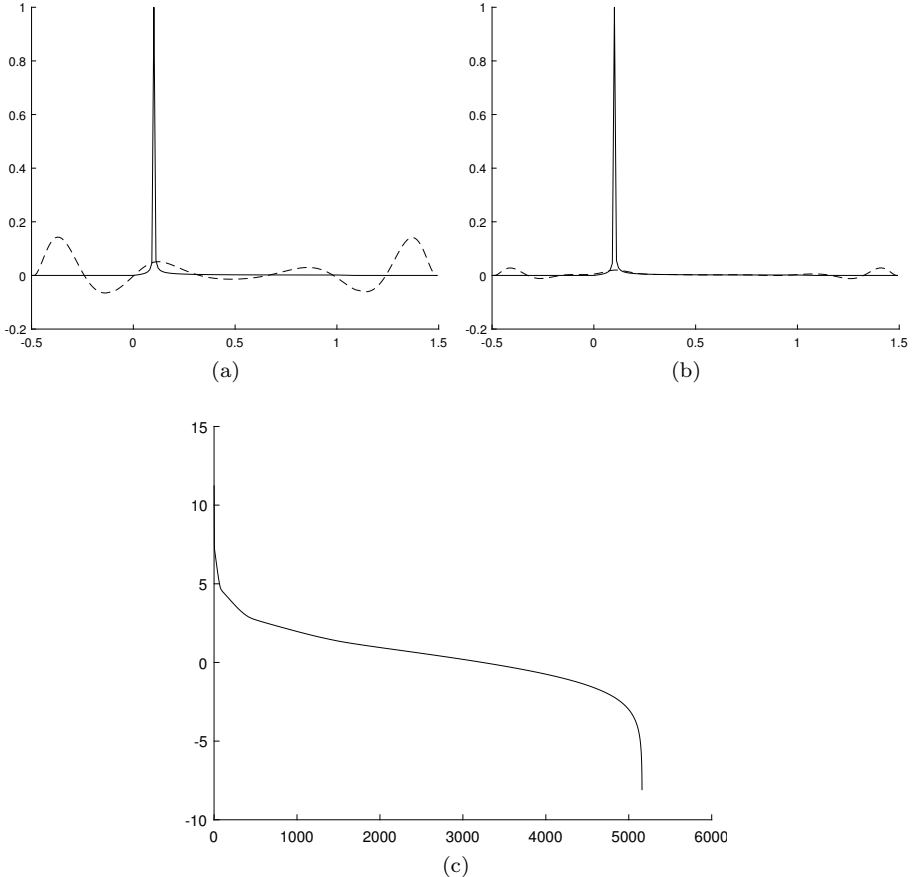


Fig. 4: The initial (a), final convergent state (b) and convergence curve in logarithmic coordinate system (c) with respect to the error for finding the optimum supporting baseline of FFT with respect to time series  $y(t) = 100 \sin 20\pi t$ . The iteration lasts for 5161 steps and costs 1.88 seconds.

**4.1 Experiments on Finding the Supporting Baseline** We choose five typical signals including single mode signal, multi-mode signal, piecewise continuous signal, signal that are not necessarily narrow-banded, composite signal in which the center frequency of its components are very close. We only illustrate the initial and final state of the iteration for the evaluation of the support baseline, as well as the convergent curve with respect to the error in logarithm to indicate the number of iteration steps in the caption, and leave the detail of decomposition result in C.

Experiment 1: The first example is a single mode signal, on the other words, the signal is narrow-banded and only contains one center frequency. Here we choose

$y(t) = 100 \sin 20\pi t$ . As we see the normalized center frequency is 0.1. The algorithm takes 5161 steps and 1.88 seconds to converge.

Experiment 2: The second example is a multi-mode signal,  $y(t) = 10 \cos(10\pi t) + 20 \sin(20\pi t)$ , which has two modes, exactly. The normalized center frequency is 0.05 and 0.1, which is relatively very close to each other. However, our algorithm can still survive where center frequencies of different modes are very close, since from 6000th iteration and on, the support baseline forms a small bulge at the close frequency points, which just separates the two frequency points.

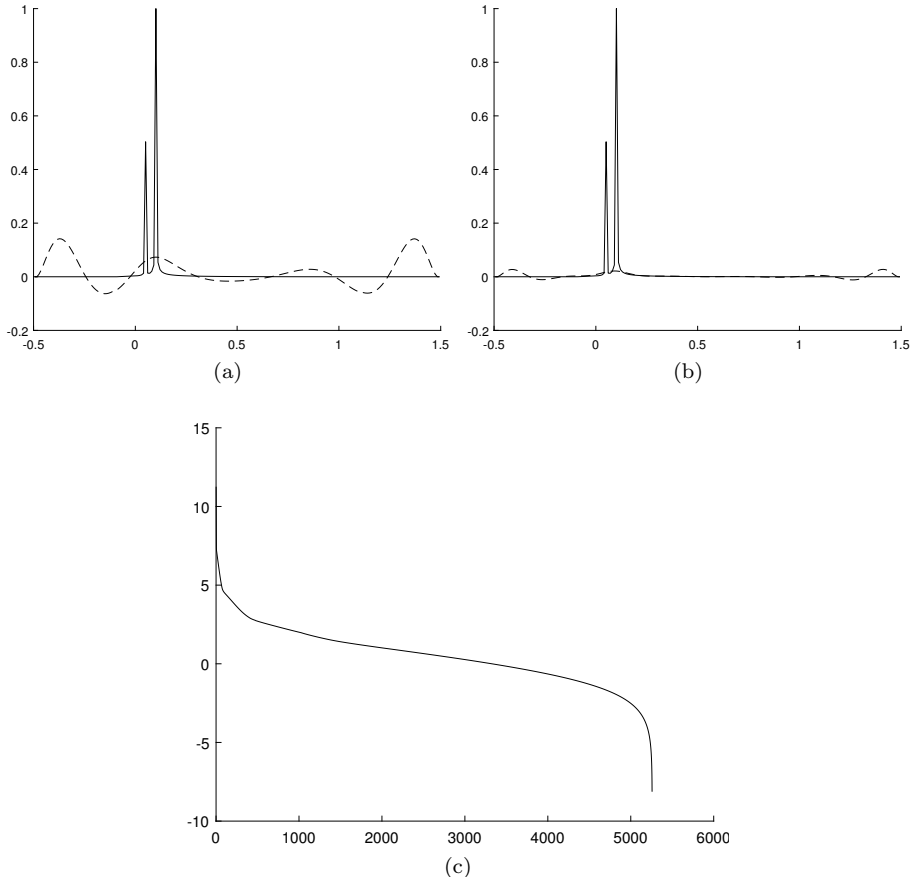


Fig. 5: The initial (a), final convergent state (b) and convergence curve in logarithmic coordinate system (c) for finding the supporting baseline of FFT with respect to FFT of  $y(t) = 10 \cos 10\pi t + 20 \sin 20\pi t$ . The iteration lasts for 5258 steps and costs 1.89 seconds.

Experiment 3: The next example is a little complicated, it has four modes totally, we choose

$$(4.1) \quad y(t) = \begin{cases} 6t^2 + \cos(10\pi t + 10\pi t^2) + \cos(60\pi t), & t \in [0, 0.5] \\ 6t^2 + \cos(10\pi t + 10\pi t^2) + \cos(80\pi t - 10\pi), & t \in (0.5, 1] \end{cases}$$

as our signal. It has a low frequency component,  $6t^2$ , two pure harmonic components,

$\cos 60\pi t, \cos(80\pi t - 10\pi)$ , in different intervals that does not intersect with each other, respectively, and one narrow banded component,  $\cos(10\pi t + 10\pi t^2)$ , in the whole interval. To our surprise, the iteration converges even more quickly than those signals that has fewer modes. In our cases, it takes about 3026 iterations to achieve the convergence.

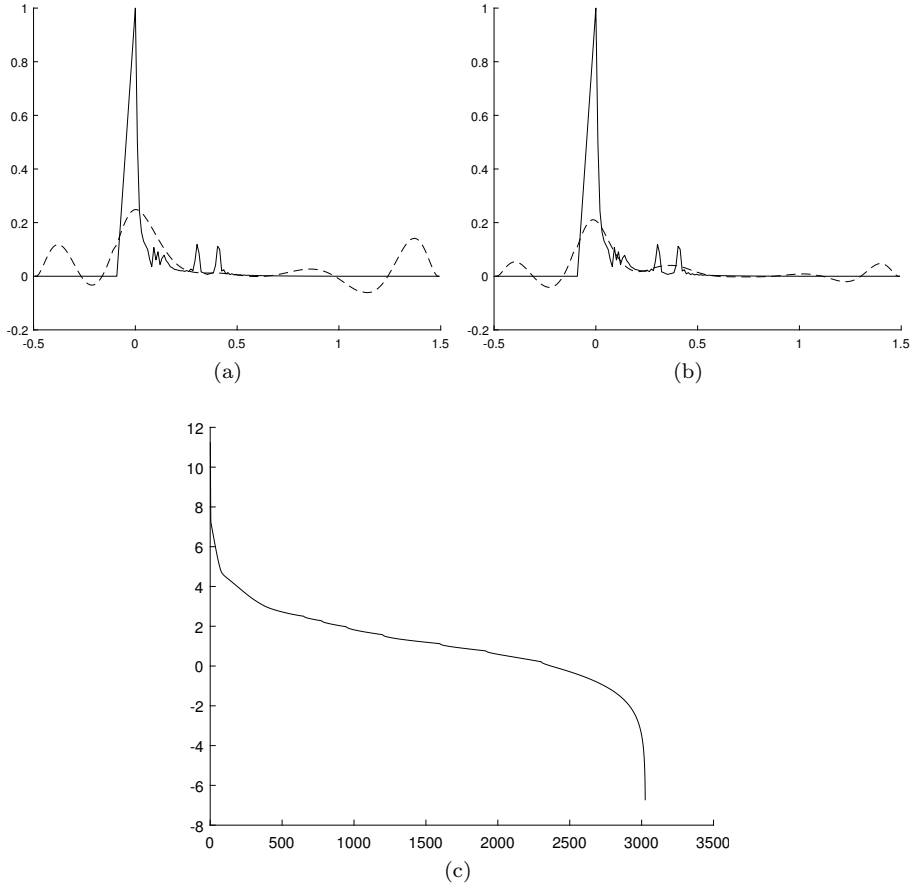


Fig. 6: The initial (a), final convergent state (b) and convergence curve in logarithmic coordinate system (c) for finding the supporting baseline of FFT with respect to time series (4.1). Note that although the spectrum of second mode,  $\cos 10\pi t$ , is affected by that of the first mode,  $6t^2$ , the computed supporting baseline precisely captured the trend of the lower bound so that all the modes can be filtered out. The iteration lasts for 3026 steps and costs 1.07 seconds.

Experiment 4: Now we show some examples on signals that conflict with the narrow-band assumption. We take  $\frac{1}{1.2 + \cos 2\pi t} + \frac{\cos(32\pi t + 0.2 \cos 64\pi t)}{1.5 + \sin(2\pi t)}$ . As we see that, the spectrum of the signal exhibits two main peaks, however the signal is not a completely narrow-band signal since it exhibits comb-shaped spectrum with respect to harmonic components, although the energy of those harmonic components are

relatively very small(Fig. 7). Our algorithm extracts three components of the signal, despite that in the mainstream view there should be only two IMFs. However, since it is not a narrow-band signal, the difficulty of decomposition objectively exists since one can not even provide a specific standard to determine whether these small harmonic components should be considered as an intrinsic mode. We also observe that, even in [5, 12] when carefully zoomed in, there does exist small oscillations in the first decomposed component which indicates the non-purity of it. Despite the fact that our results has three components, every separate component exhibits better purity than the pioneer works. On the other side, from the perspective of reconstruction error, it is shown in this example that, results generated by algorithm in [5] with both 2 and 3 modes has reconstruction error as twice as large as ours, which also indicates that our algorithm has better performance in this case.

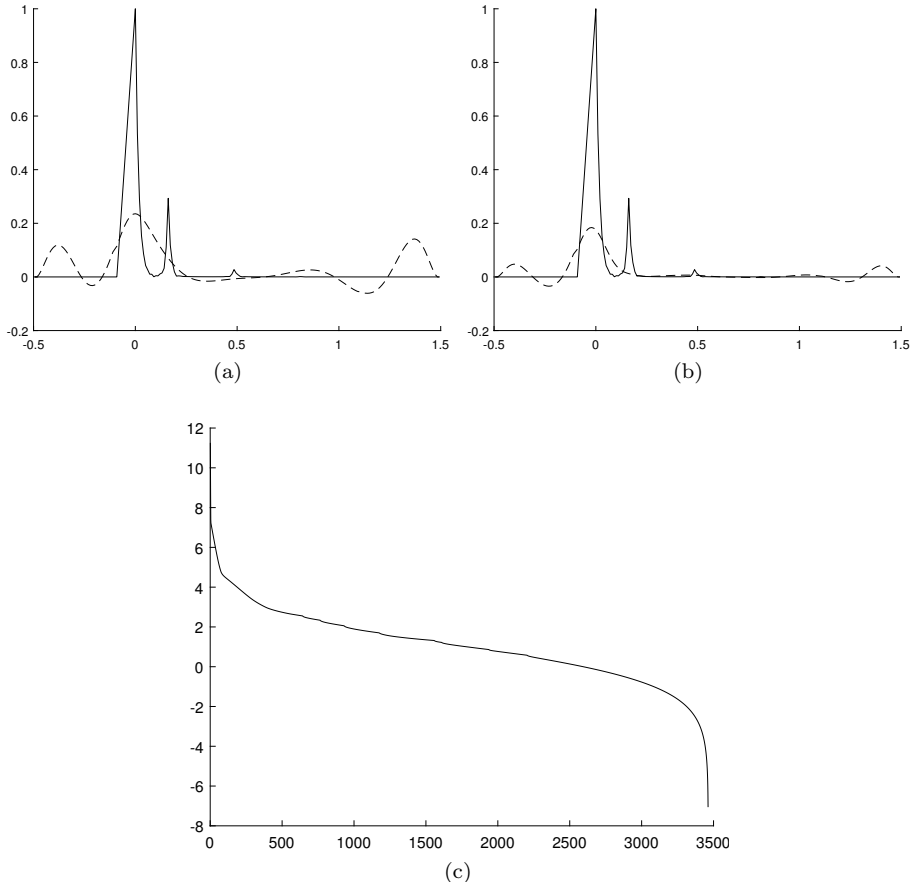
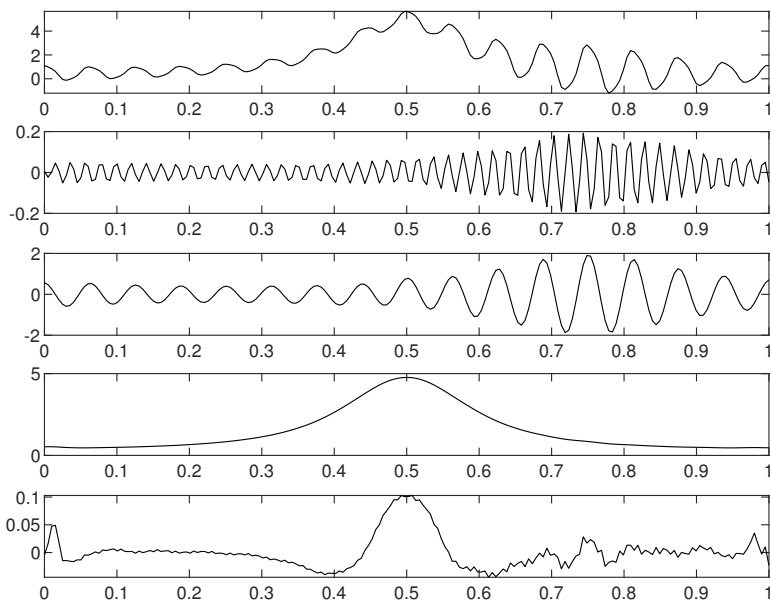
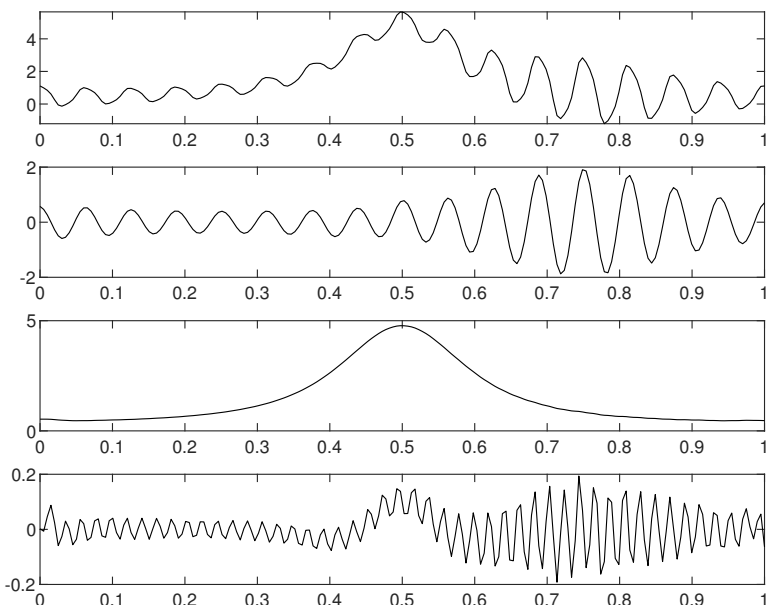


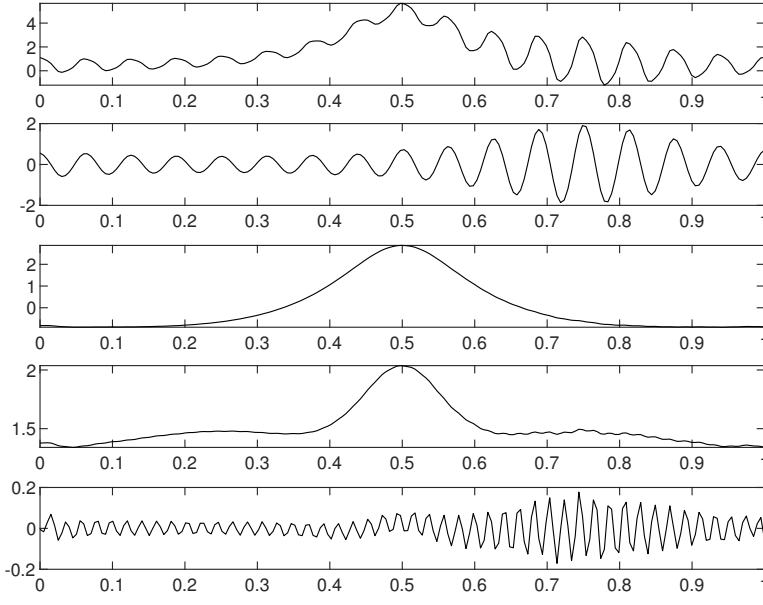
Fig. 7: The initial (a), final convergent state (b) and convergence curve in logarithmic coordinate system (c) for finding the baseline of function  $\frac{1}{1.2+\cos 2\pi t} + \frac{\cos(32\pi t+0.2 \cos 64\pi t)}{1.5+\sin(2\pi t)}$ . The iteration lasts for 3463 steps and costs 1.25 seconds.



(a)



(b)



(c)

Fig. 7: The decomposition result (a) of  $\frac{1}{1.2 + \cos 2\pi t} + \frac{\cos(32\pi t + 0.2 \cos 64\pi t)}{1.5 + \sin(2\pi t)}$  from the subsequent VMD, using the found number of modes and center frequency as initialization, compared with original VMD results with IMFS number 2 (b) and 3 (c) respectively. The sub-figure from top to bottom are respectively the source signal, the decomposed modes (there are three) and the residual. As compared with (b) and (c), for original VMD, both the results has reconstruction error twice as large as ours.

Experiment 5: Next we show even when the central frequencies are very close, our algorithm can also work well. We take signals as  $y(t) = 6t + \sum_{i=1}^{10} (13-i) \cos[(20+10i)\pi t]$ . The signal has one low-frequency component and 10 alternating current components with different amplitudes, of which the minimum difference between frequency gaps is only 0.04 after normalization and our algorithm can still survive in figuring out all the components.

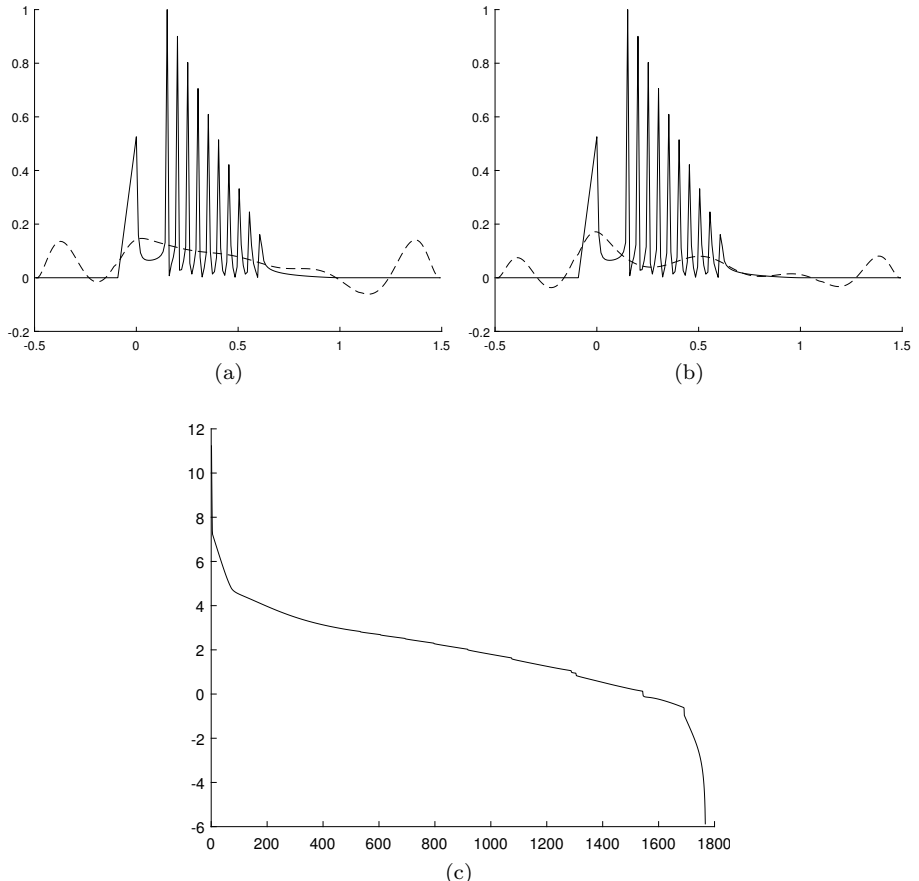


Fig. 8: The initial (a), final convergent state (b) and convergence curve in logarithmic coordinate system (c) for finding the baseline of function  $y(t) = 6t + \sum_{i=1}^{10} (13 - i) \cos[(20 + 10i)\pi t]$ , The iteration lasts for 1768 steps and costs 0.64 seconds.

**4.2 Experiments on Central Frequencies** In order to prove that our algorithm can find frequencies close to the practical central frequencies for each IMF component, we compare our results from the above Example 1 to Example 5, with the results of the original VMD process with the same number of IMF, to keep away the impact to the performance of VMD from the initial frequency value that we provide to the following VMD procedure. We first get the frequency estimation from our algorithm and the result of pure VMD procedure with the same number of IMFs respectively, and then sort them in order, to observe the difference between the results of ours and the corresponding values from VMD.

Table 1: The evaluated center frequencies

Experiment	Ours	Original VMD	Max Difference
1	0.0550	0.0496	0.0054
2	0.0300, 0.0575	0.0251, 0.0507	0.0068
3	0.0100, 0.0775 0.1550, 0.2075	0.0008, 0.0530 0.1510, 0.2	0.0245
4	0.0125, 0.0875 0.2475	6.46e-5, 0.0067 0.0803	0.1682
5	0.005, 0.0775 0.1, 0.125 0.1550, 0.1800 0.2075, 0.2325 0.2575, 0.2825 0.3075	0.000845, 0.0747 0.0999, 0.1250 0.1510, 0.182 0.223, 0.25 0.2760, 0.303 0.339	0.0315

Table 1 shows the result, where in each experiment the evaluated center frequencies for both ours and the pure VMD are sorted, and the max difference is computed as  $\max_i |f_i - F_i|$ , where  $f$  stands for our estimated frequencies and  $F$  pure VMD's. As shown in Table 1, in most cases, our estimation to the center frequencies has low difference with respect to the pure VMD. It can be found that, in Experiment 4, the error between estimated center frequencies of ours and pure VMD's are larger than the average, however, as analysed in Experiment 4, on one side, the original VMD, no matter given IMFs number 2 or 3, fails to achieve reconstruction error as small as ours, on the other side, as shown in Fig.7c even when both started at IMFs number 3, the original VMD seems produce replicated modes at the Gaussian-alike component, with almost the same amplitude and shape, while ours provide relatively independent components when given our initial estimation for the center frequencies, which seems to indicates that our estimation in this case is more reliable.

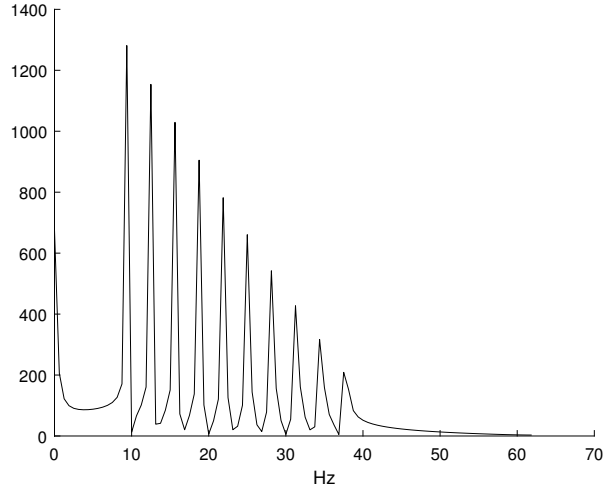


Fig. 9: The original spectrums for signal  $y(t) = 6t + \sum_{i=1}^{10} (13 - i) \cos[(20 + 10i)\pi t]$ .

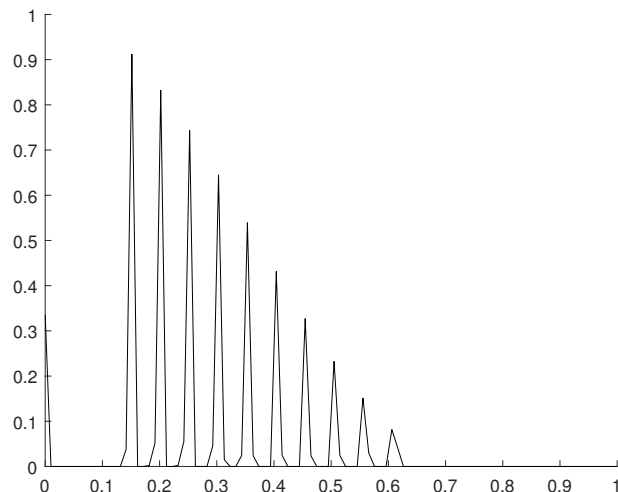


Fig. 10: The decomposed spectrums for signal  $y(t) = 6t + \sum_{i=1}^{10} (13 - i) \cos[(20 + 10i)\pi t]$  by our method.

#### 4.3 Experiments Compared with Variational Mode Decomposition

We noticed that, the Successive Variational Mode Decomposition(SVMD) method is another competitive method that can also automatically determine the number of IMFs for VMD[12] without any prior knowledge although it also lacks of rigorous proof on the convergence. This method retrieves the modes one after another by recursively

finding the  $L$ th mode from the residual, assuming the first  $L - 1$  modes are found after the last turn, until the final residual can be ignored with respect to some criterion set by the algorithm. However, since the method is in essence recursive, the accuracy for the next mode to be evaluated is highly depended on the residual determined by previous decomposition in all former turns, which will inevitably introduce accumulated error during the propagation. We used official MATLAB implementation on SVMD [25] and observed that for narrow-banded signals wherein the center frequencies of different components are very close, the SVMD method may either introduce some redundant modes or drop some significant modes in their decomposition results, yet the phenomenon is hardly observed in our algorithm.

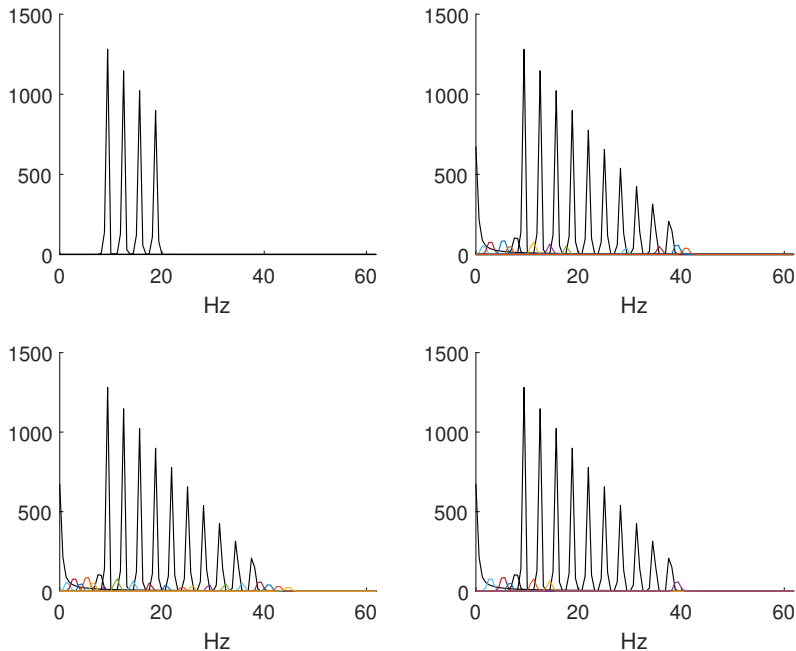


Fig. 11: The decomposed spectrums for signal  $y(t) = 6t + \sum_{i=1}^{10} (13 - i) \cos[(20 + 10i)\pi t]$  by SVMD under different stopping criteria by considering noise(northwest), exact decomposition(northeast), Bayesian Estimation(southwest), power of the last mode(southeast).

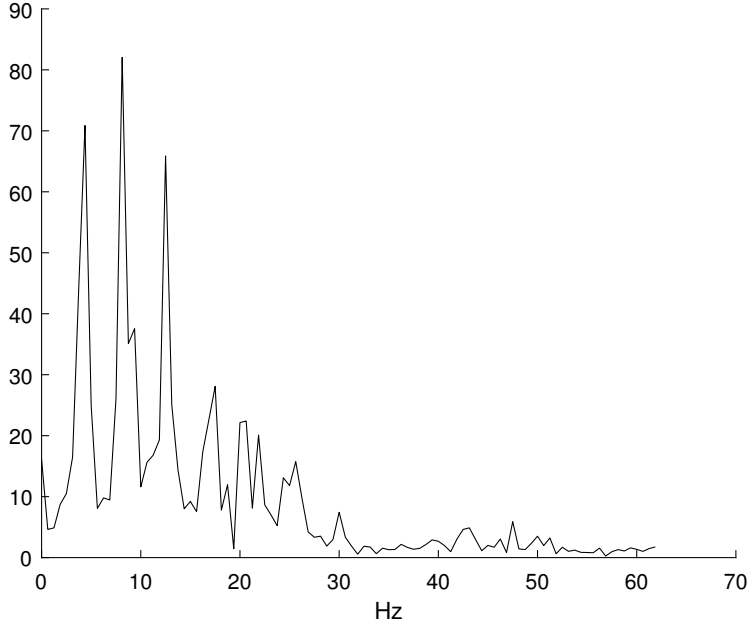


Fig. 12: The original spectra for signal of the 102th record in MIT-BIH Arrhythmia Database.

In this section, we pick 2 typical signals for illustration. The first one is  $y(t) = 6t + \sum_{i=1}^{10} (13 - i) \cos[(20 + 10i)\pi t]$ , which we have investigated in the experiments for finding the supporting baseline. For the completeness of our comparison, we investigated all stopping criterion implemented in the source code of SVMD. The method considering about eliminating noise(northwest) drops the base-frequency and a batch of high frequency, while method for extract reconstruction, method based on Bayesian Estimation, or method considering the power of last mode all result in some redundant modes with low energy on the decomposed spectrum (see colored spectrum at the bottom in each subplot), which are not the essential modes that should included in the decomposition result (Fig. 11). In contrast, our method(Fig. 10) accurately extracts all necessary modalities without any redundant ones.

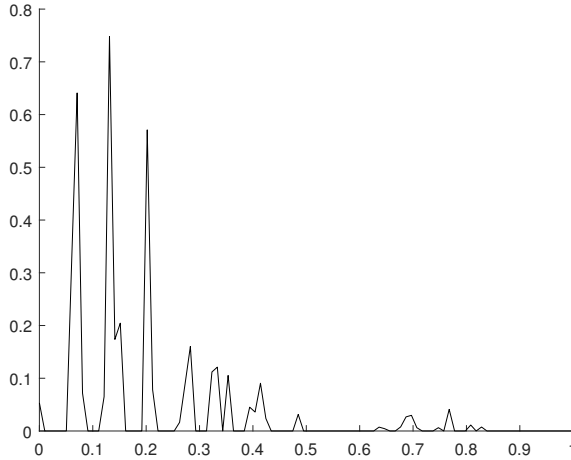


Fig. 13: The decomposed spectrums for the V2 lead of the 102th record in MIT-BIH Arrhythmia Database by our method.

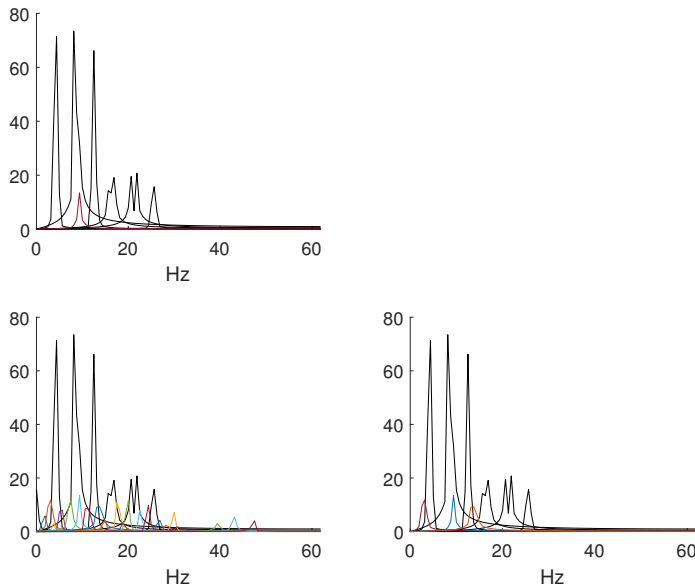


Fig. 14: The decomposed spectrums for signal with respect to the V2 lead of the 102th record in MIT-BIH Arrhythmia Database, and decomposed by [25] under different stopping criteria by considering noise(northwest), Bayesian Estimation(southwest), power of the last mode(southeast). Note that the figure for the exact decomposition is missed since the SVMD failed to converge in 10 seconds.

The second one is ECG signals from V2 lead of the 102th record in MIT-BIH Arrhythmia Database [23, 24]. The experiment result also shows similar phenomenon as stated in the former experiment, the method for exact decomposition fails to converge in more than 10 seconds so we cannot draw the spectrum of the corresponding figure

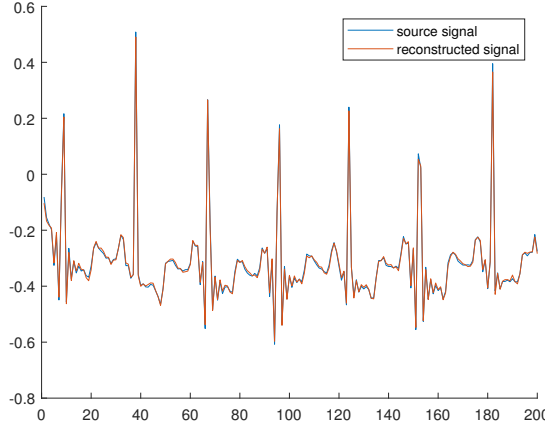


Fig. 15: The source signal (blue line) and the reconstructed signal (orange line) from the sum of IMFs obtained from our algorithm with respect to MLII lead from the 100th record.

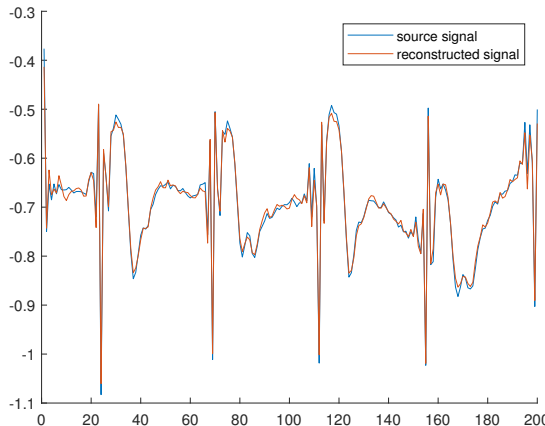


Fig. 16: The source signal (blue line) and the reconstructed signal (orange line) from the sum of IMFs obtained from our algorithm with respect to V4 lead from the 124th record.

(Fig. 14). Our method in this case can also succeed in retrieving all the effective modes (Fig. 13).

**4.4 Experiment on Real Signals** In this section we investigate the performance of our method on real signals. As ECG signals are typical ones that combined with several narrow-banded components, we choose ECG signals as real signals for verification. Our ECG signals derives from MIT-BIH Arrhythmia Database [23, 24], and we choose randomly two signals for analysis, wherein the first is the MLII lead

from the 100th record and the second is the V4 lead from the 124th record for our experiments respectively. Since each original signal has about 65000 samples which makes redundant for our experiment, we choose the first 2000 samples and do down-sampling at the ratio 1:10 for computation efficiency. For the limitation of the page we put the course of iteration and the decomposition result in Supplementary Materials (Fig. S3.16, Fig. S3.17 and Fig. S3.18, Fig. S3.19 for iteration and decomposition result with respect to the first and second chosen signals respectively), and instead we analyse the correlation coefficient(CC, the higher the better) and the ratio between the power ratio(PR) with respect to the residual and the original signal(the lower the better), and illustrate the gap between the reconstructed signal from the sum of the IMFs that acquired by our algorithm and the source signal.

For real signals composed of narrow-banded components, our algorithm can obtain effective components, since on one side the gap between the source signal(solid line in Fig. 15 and Fig. 16) and reconstructed signal(dashed line in Fig. 15 and Fig. 16) is typically small, meaning that one can always revive the source signal with small error by adding all the IMFs obtained from algorithm. On the other side, as shown in Table 2, the sum of IMF components obtained by our algorithm can achieve high correlation coefficient(both over 0.99) and low power ratio with respect to residual and the source signal(at the order of  $10^{-4}$ ), which indicates our algorithm can automatically retrieve almost all the meaningful components to the source signal and seldom ignore the significance of components with small energy.

Table 2: The number of IMFs acquired from our algorithm, the CC(Correlation Coefficients between the reconstructed signal and source signal) and the PR(Power Ratio with respect to the residual and the source signal) result.

Experiment	Number of IMFs	CC	PR
MLII lead from the 100th record	15	0.9989	4.2635e-04
V4 lead from the 124th record	14	0.9959	2.0626e-04

**5 Conclusion** In this article, we proposed a globally convergent method that can automatically determine the number of intrinsic mode functions for Variational Mode Decomposition. For narrow-banded signals, this method does not need any prior knowledge about the scope of the IMFs number, and provide non-recursively schema to determine IMFs and corresponding central frequencies simultaneously. Experiments show that, our method can provide accurate number of IMFs and corresponding center frequencies even if the center frequencies are very close. Our implementation is performant in both accuracy and speed. Moreover, rigorous proof is given for the convergence of the method, making it theoretically reliable.

**6 Acknowledgement** This study is supported by the National Natural Science Foundation of China under Grant No. 61773290 and the Fundamental Research Funds for the Central Universities (22120230311).

## REFERENCES

- [1] G. BALDINI AND F. BONAVITACOLA, *Channel identification with improved variational mode decomposition*, Physical Communication, 55 (2022), p. 101871, <https://doi.org/https://doi.org/10.1016/j.phycom.2022.101871>, <https://www.sciencedirect.com/science/article/pii/S1874490722001495>.
- [2] D. BERTSEKAS, *Convex Optimization Algorithms*, Athena Scientific, 2015, <https://books.google.com.sg/books?id=OwQ7EAAAQBAJ>.
- [3] W. E. BOYCE, R. C. DiPRIMA, AND D. B. MEADE, *Boyce's elementary differential equations and boundary value problems*, 2017 - 2017.
- [4] S. BOYD AND L. VANDENBERGHE, *Convex Optimization*, Cambridge University Press, 2004.
- [5] K. DRAGOMIRETSKIY AND D. ZOSO, *Variational mode decomposition*, IEEE Transactions on Signal Processing, 62 (2014), pp. 531–544, <https://doi.org/10.1109/TSP.2013.2288675>.
- [6] Z. FENG, D. ZHANG, AND M. J. ZUO, *Adaptive mode decomposition methods and their applications in signal analysis for machinery fault diagnosis: A review with examples*, IEEE Access, 5 (2017), pp. 24301–24331, <https://doi.org/10.1109/ACCESS.2017.2766232>.
- [7] G. KUMARAGURUPARAN AND M. K. HOTA, *Microseismic signal denoising based on variational mode decomposition with adaptive non-local means filtering*, Pure and Applied Geophysics, 180 (2023), pp. 1–23, <https://doi.org/10.1007/s00024-023-03365-0>.
- [8] D. LAO, *Fundamentals of the Calculus of Variations(3rd Edition)*, National Defense Industry Press, 2015.
- [9] C. LI, Y. WU, H. LIN, J. LI, F. ZHANG, AND Y. YANG, *Ecg denoising method based on an improved vmd algorithm*, IEEE Sensors Journal, 22 (2022), pp. 22725–22733, <https://doi.org/10.1109/JSEN.2022.3214239>.
- [10] Y. LI, D. HUANG, AND Z. QIN, *A classification algorithm of fault modes-integrated lssvm and pso with parameters' optimization of vmd*, Mathematical problems in engineering, 2021 (2021), p. 6627367.
- [11] J. LIAN, Z. LIU, H. WANG, AND X. DONG, *Adaptive variational mode decomposition method for signal processing based on mode characteristic*, Mechanical Systems and Signal Processing, 107 (2018), pp. 53–77, <https://doi.org/10.1016/j.ymssp.2018.01.019>.
- [12] M. NAZARI AND S. M. SAKHAEI, *Successive variational mode decomposition*, Signal Processing, 174 (2020), p. 107610, <https://doi.org/https://doi.org/10.1016/j.sigpro.2020.107610>, <https://www.sciencedirect.com/science/article/pii/S0165168420301535>.
- [13] N. U. REHMAN AND H. AFTAB, *Multivariate variational mode decomposition*, IEEE Transactions on Signal Processing, 67 (2019), pp. 6039–6052, <https://doi.org/10.1109/TSP.2019.2951223>.
- [14] V. SHARMA, *Gear fault detection based on instantaneous frequency estimation using variational mode decomposition and permutation entropy under real speed scenarios*, Wind Energy, 24 (2020), <https://doi.org/10.1002/we.2570>.
- [15] THEORETICAL AND C. B. GROUP, *For more information on vmd and mdscope*, <https://www.ks.uiuc.edu/Research/vmd/vmd-1.3/ug/node5.html>.
- [16] B. WEN-CHAO, S. LIANG-DUO, C. LIANG, AND X. CHU-TIAN, *Monthly runoff prediction based on variational modal decomposition combined with the dung beetle optimization algorithm for gated recurrent unit model*, Environmental Monitoring and Assessment, 195 (2023), <https://doi.org/10.1007/s10661-023-12102-y>.
- [17] S. WU, F. FENG, J. ZHU, C. WU, AND G. ZHANG, *A method for determining intrinsic mode function number in variational mode decomposition and its application to bearing vibration signal processing*, Shock and Vibration, 2020 (2020), pp. 1–16, <https://doi.org/10.1155/2020/8304903>.
- [18] Y.-K. XIA, W.-T. WANG, AND X.-Y. LI, *Adaptive parameter selection variational mode decomposition based on bayesian optimization and its application to the detection of itsc in pmsm*, IEEE Access, PP (2024), pp. 1–1, <https://doi.org/10.1109/ACCESS.2024.3373880>.
- [19] J. YANG, E. STEWART, J. YE, M. ENTEZAMI, AND C. ROBERTS, *An improved vmd method for use with acoustic impact response signals to detect corrosion at the underside of railway tracks*, Applied Sciences, 13 (2023), p. 942, <https://doi.org/10.3390/app13020942>.
- [20] D. YU AND H. TANG, *Numerical Solutions of Differential Equations*, Science Press, 2018.
- [21] S. ZHANG, G. LIU, R. XIAO, W. CUI, J. CAI, X. HU, Y. SUN, J. QIU, AND Y. QI, *A combination of statistical parameters for epileptic seizure detection and classification using vmd and nltwsvm*, Biocybernetics and Biomedical Engineering, 42 (2022), pp. 258–272, <https://doi.org/https://doi.org/10.1016/j.bbce.2022.02.004>, <https://www.sciencedirect.com/science/article/pii/S0208521622000079>.
- [22] Q. ZHENG, T. CHEN, L. XIE, AND H. SU, *Short-time variational mode decomposition: Algorithm and applications*, <https://doi.org/10.1007/s10661-023-12102-y>.

*rithms, extensions and properties*, SSRN Electronic Journal, (2022), <https://doi.org/10.2139/ssrn.4080800>.

- [23] MOODY GB, MARK RG. THE IMPACT OF THE MIT-BIH ARRHYTHMIA DATABASE. IEEE ENG IN MED AND BIOL 20(3):45-50 (MAY-JUNE 2001). (PMID: 11446209).
- [24] GOLDBERGER, A. L., AMARAL, L. A., GLASS, L., HAUSDORFF, J. M., IVANOV, P. C., MARK, R. G., MIETUS, J. E., MOODY, G. B., PENG, C. K., & STANLEY, H. E. (2000). PHYSIOBANK, PHYSIOToolkit, and PhysioNet: Components of a New Research Resource for Complex Physiologic Signals. CIRCULATION, 101(23), E215-E220. [HTTPS://DOI.ORG/10.1161/01.CIR.101.23.E215](https://doi.org/10.1161/01.CIR.101.23.E215).
- [25] Mojtaba Nazari (2026). Successive Variational Mode Decomposition (SVMD.m) <https://ww2.mathworks.cn/matlabcentral/fileexchange/98649-successive-variational-mode-decomposition-svmd-m>, MATLAB Central File Exchange.
- [26] COLLINS, P. J. (2006). *Differential and Integral Equations*. OXFORD UNIVERSITY PRESS, OXFORD, UK.
- [27] KRESS, R. (2013). *Linear Integral Equations*. APPLIED MATHEMATICAL SCIENCES, SPRINGER NEW YORK.
- [28] KEENER, J. P. (2019). *Principles Of Applied Mathematics: Transformation and Approximation*. CRC PRESS.

**Appendix A. Finite Discrete Expression and Their Matrices.** Here we show finite discrete expression and the corresponding the conversion matrices with respect to (2.11),(2.12). Since the finite difference expressions for  $\alpha(x)$  and  $g(x)$  are identical in form, the conversion matrices  $\mathbf{G}^{(n)}$  and  $\mathbf{A}^{(n)}$  also share the exactly the same structure

$$(S1.1) \quad g^{(1)}(x) \approx \frac{-g(x+2h) + 8g(x+h) - 8g(x-h) + g(x-2h)}{12h}$$

$$(S1.2) \quad g^{(2)}(x) \approx \frac{-g(x+2h) + 16g(x+h) - 30g(x) + 16g(x-h) - g(x-2h)}{12h^2}$$

$$(S1.3) \quad g^{(3)}(x) \approx \frac{g(x+2h) - 2g(x+h) + 2g(x-h) - g(x-2h)}{2h^3}$$

$$(S1.4) \quad g^{(4)}(x) \approx \frac{g(x+2h) - 4g(x+h) + 6g(x) - 4g(x-h) + g(x-2h)}{h^4}$$

$$(S1.5) \quad \mathbf{A}^{(1)} = \mathbf{G}^{(1)} = \frac{1}{12} \begin{bmatrix} 1 & -8 & 0 & 8 & -1 & 0 & \dots & \dots & \dots & 0 \\ 0 & 1 & -8 & 0 & 8 & -1 & 0 & \dots & \dots & 0 \\ \vdots & \vdots \\ 0 & \dots & \dots & 0 & 1 & -8 & 0 & 8 & -1 & 0 \\ 0 & 0 & \dots & \dots & 0 & 1 & -8 & 0 & 8 & -1 \end{bmatrix}$$

$$(S1.6) \quad \mathbf{A}^{(2)} = \mathbf{G}^{(2)} = \frac{1}{12} \begin{bmatrix} -1 & 16 & -30 & 16 & -1 & 0 & \dots & \dots & \dots & 0 \\ 0 & -1 & 16 & -30 & 16 & -1 & 0 & \dots & \dots & 0 \\ \vdots & \vdots \\ 0 & \dots & \dots & 0 & -1 & 16 & -30 & 16 & -1 & 0 \\ 0 & 0 & \dots & \dots & 0 & -1 & 16 & -30 & 16 & -1 \end{bmatrix}$$

$$(S1.7) \quad \mathbf{A}^{(3)} = \mathbf{G}^{(3)} = \frac{1}{2} \begin{bmatrix} -1 & 2 & 0 & -2 & 1 & 0 & \dots & \dots & \dots & 0 \\ 0 & -1 & 2 & 0 & -2 & 1 & 0 & \dots & \dots & 0 \\ \vdots & \vdots \\ 0 & \dots & \dots & 0 & -1 & 2 & 0 & -2 & 1 & 0 \\ 0 & 0 & \dots & \dots & 0 & -1 & 2 & 0 & -2 & 1 \end{bmatrix}$$

$$(S1.8) \quad \mathbf{A}^{(4)} = \mathbf{G}^{(4)} = \begin{bmatrix} 1 & -4 & 6 & -4 & 1 & 0 & \dots & \dots & \dots & 0 \\ 0 & 1 & -4 & 6 & -4 & 1 & 0 & \dots & \dots & 0 \\ \vdots & \vdots \\ 0 & \dots & \dots & 0 & 1 & -4 & 6 & -4 & 1 & 0 \\ 0 & 0 & \dots & \dots & 0 & 1 & -4 & 6 & -4 & 1 \end{bmatrix}$$

and after evaluating  $(2\mathbf{A}^{(2)}\boldsymbol{\alpha}) \odot \mathbf{G}^{(2)} + (4\mathbf{A}^{(1)}\boldsymbol{\alpha}) \odot \mathbf{G}^{(3)} + 2\boldsymbol{\alpha} \odot \mathbf{G}^{(4)}$ , we introduce another 4 lines depicting the boundary value condition, noted as  $\mathbf{B}$ :

$$(S1.9) \quad \mathbf{B} = \begin{bmatrix} 1 & 0 & 0 & \cdots & \cdots & 0 & 0 & 0 \\ 0 & 0 & 0 & \cdots & \cdots & 0 & 0 & 1 \\ -1 & 1 & 0 & \cdots & \cdots & 0 & 0 & 0 \\ 0 & 0 & 0 & \cdots & \cdots & 0 & -1 & 1 \end{bmatrix}$$

and (2.11) is then transformed into

$$(S1.10) \quad \begin{bmatrix} (2\mathbf{A}^{(2)}\boldsymbol{\alpha}) \odot \mathbf{G}^{(2)} + (4\mathbf{A}^{(1)}\boldsymbol{\alpha}) \odot \mathbf{G}^{(3)} + 2\boldsymbol{\alpha} \odot \mathbf{G}^{(4)} \\ \mathbf{B} \end{bmatrix} \mathbf{g} = \mathbf{c}$$

in which

$$(S1.11) \quad \boldsymbol{\alpha} = \begin{bmatrix} \alpha_0 \\ \alpha_1 \\ \vdots \\ \alpha_{N-1} \\ \alpha_N \end{bmatrix}, \mathbf{g} = \begin{bmatrix} g_0 \\ g_1 \\ \vdots \\ g_{N-1} \\ g_N \end{bmatrix} \text{ and } \mathbf{c} = \begin{bmatrix} h^4 c_2 \\ h^4 c_3 \\ \vdots \\ h^4 c_{N-3} \\ h^4 c_{N-2} \\ c_0 \\ c_N \\ c_1 - c_0 \\ c_N - c_{N-1} \end{bmatrix}$$

and  $c_i = \beta_i - \lambda_i + \mu_i$ . In this way the condition number of the matrix to be inverted during evaluation is more gentle.

## Appendix B. Supplementary Material of the Proof.

**B.1 Proof of Convexity** Let  $\mathcal{O}(g(x)) = \mathcal{O}_1(g(x)) + \mathcal{O}_2(g(x))$ , where  $\mathcal{O}_1(g(x)) = \int_{\Omega} \alpha(x) g''^2(x) dx$  and  $\mathcal{O}_2(g(x)) = - \int_{\Omega} \beta(x) g(x) dx$ . For  $\mathcal{O}_1(g(x))$ , we have

$$(S2.1) \quad \begin{aligned} \lambda \mathcal{O}_1(g_1(x)) + (1 - \lambda) \mathcal{O}_1(g_2(x)) - \mathcal{O}_1[\lambda g_1(x) + (1 - \lambda) g_2(x)] \\ = \lambda(1 - \lambda) \int_{\Omega} \alpha(x) [g_1''(x) - g_2''(x)]^2 dx \geq 0 \end{aligned}$$

and  $\mathcal{O}_2(g(x))$  is obviously a linear functional, so we have

$$(S2.2) \quad \mathcal{O}[\lambda g_1(x) + (1 - \lambda) g_2(x)] \leq \lambda \mathcal{O}[g_1(x)] + (1 - \lambda) \mathcal{O}[g_2(x)]$$

so that our objective functional is convex.

**B.2 Concavity of Dual Functional  $\mathcal{G}$**  In this part we give a short proof to the concavity of  $\mathcal{G}$ . According to the definition of  $\mathcal{G}$ , we have

$$\begin{aligned}
 (S2.3) \quad & \mathcal{G}(\theta\lambda_1(x) + (1-\theta)\lambda_2(x), \theta\mu_1(x) + (1-\theta)\mu_2(x)) \\
 &= \inf_{g(x) \in \mathcal{D}} \mathcal{L}[g(x), \theta\lambda_1(x) + (1-\theta)\lambda_2(x), \theta\mu_1(x) + (1-\theta)\mu_2(x)] \\
 &= \inf_{g(x) \in \mathcal{D}} \mathcal{L}[\theta g(x) + (1-\theta)g(x), \theta\lambda_1(x) + (1-\theta)\lambda_2(x), \theta\mu_1(x) + (1-\theta)\mu_2(x)] \\
 &= \inf_{g(x) \in \mathcal{D}} \{\theta\mathcal{L}[g(x), \lambda_1(x), \mu_1(x)] + (1-\theta)\mathcal{L}[(g(x), \lambda_2(x), \mu_2(x)]\} \\
 &\geq \theta \inf_{g(x) \in \mathcal{D}} \mathcal{L}[g(x), \lambda_1(x), \mu_1(x)] + (1-\theta) \inf_{g(x) \in \mathcal{D}} \mathcal{L}[g(x), \lambda_2(x), \mu_2(x)] \\
 &= \theta\mathcal{G}(\lambda_1(x), \mu_1(x)) + (1-\theta)\mathcal{G}(\lambda_2(x), \mu_2(x))
 \end{aligned}$$

which concludes the concavity of  $\mathcal{G}$ .

**B.3 Proof of the Zero Duality Gap** Now we begin to prove that the duality gap is zero. Let

$$(S2.4) \quad \mathcal{O}(g(x)) = \int_{\Omega} \alpha(x)g''^2(x)dx - \int_{\Omega} \beta(x)g(x)dx$$

be the objective functional, and construct Lagrangian functional

$$\begin{aligned}
 (S2.5) \quad \mathcal{L}(g(x), \lambda(x), \mu(x)) &= \int_{\Omega} \alpha(x)g''^2(x)dx - \int_{\Omega} \beta(x)g(x)dx \\
 &\quad + \int_{\Omega} \lambda(x)[g(x) - f(x)]dx - \int_{\Omega} \mu(x)g(x)dx
 \end{aligned}$$

define dual functional as

$$(S2.6) \quad \mathcal{G}(\lambda(x), \mu(x)) = \inf_{g(x) \in \mathcal{D}} \mathcal{L}(g(x), \lambda(x), \mu(x))$$

then on one side, we must have

$$(S2.7) \quad \mathcal{G}(\lambda^*(x), \mu^*(x)) = \inf_{g(x)} \mathcal{L}(g(x), \lambda^*(x), \mu^*(x)) \leq \inf_{g(x)} \mathcal{O}(g(x)) = \mathcal{O}(g^*(x))$$

where  $*$  stands for the optimum. On the other hand, one can construct general sets

$$(S2.8) \quad \mathcal{S} = \{(p(x), q(x), o) | g(x) - f(x) \leq p(x), -g(x) \leq q(x), \mathcal{O}(g(x)) \leq o\}$$

which forms an epi-graph to (2.2). thus

$$(S2.9) \quad \forall \xi(x) = \lambda(p_1(x), q_1(x), o_1) + (1-\lambda)(p_2(x), q_2(x), o_2)$$

one can always find

$$(S2.10) \quad \eta(x) = \lambda g_1(x) + (1-\lambda)g_2(x)$$

that makes

$$(S2.11) \quad \begin{cases} \eta(x) - f(x) \leq \lambda p_1(x) + (1-\lambda)p_2(x) \\ -\eta(x) \leq \lambda q_1(x) + (1-\lambda)q_2(x) \\ \mathcal{O}(\eta(x)) \leq \lambda \mathcal{O}(g_1(x)) + (1-\lambda)\mathcal{O}(g_2(x)) \leq \lambda o_1 + (1-\lambda)o_2 \end{cases}$$

hold and thus  $\mathcal{S}$  is a convex set. It is obvious that  $(0, 0, \mathcal{O}(g^*(x))) \in \partial\mathcal{S}$ , so according to the Support Theorem of Convex Sets there must be a general hyperplane that on one side pass through  $(0, 0, \mathcal{O}(g^*(x))) \in \partial\mathcal{S}$  and on the other side ensures any point in  $\mathcal{S}$  locates above the hyperplane. That is, there exists  $\lambda(x), \mu(x)$  that makes

$$(S2.12) \quad \int_{\Omega} \lambda(x)p(x)dx + \int_{\Omega} \mu(x)q(x)dx \geq \mathcal{O}(g^*(x)) - o$$

hold for all  $(p(x), q(x), o)$  in  $\mathcal{S}$ . Note that for  $p(x), q(x) \geq 0$ , there exist points in  $\mathcal{S}$  that makes  $o \leq \mathcal{O}(g^*(x))$ , so there exists points that makes the right side of (S2.12) non-negative, this forces  $\lambda(x) \geq 0$  and  $\mu(x) \geq 0$ , which indicates we can find a solution in dual space making the dual-gap vanish.

Next we prove the convexity of our feasible domain. The feasible set is  $0 \leq g(x) \leq f(x)$ , so that  $\forall g_1(x), g_2(x) \in [0, f(x)]$ , we have  $\lambda g_1(x) + (1 - \lambda)g_2(x) \in [0, f(x)]$ ,  $\forall \lambda \in [0, 1]$ , which means the feasible set is also convex.

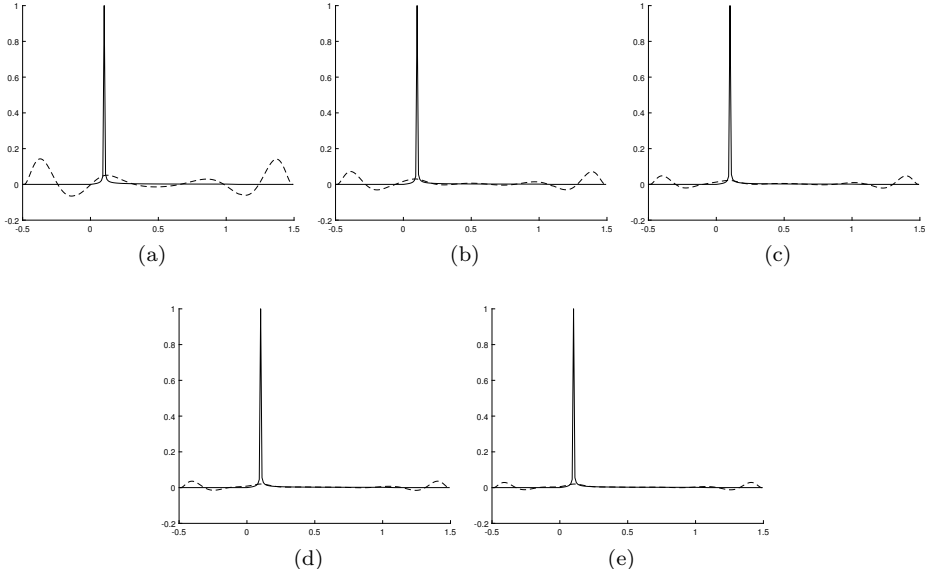


Fig. S2.1: The iteration for finding the supporting baseline of FFT with respect to time series  $y(t) = 100 \sin 20\pi t$ . The 1000th(a), 2000th(b), 3000th(c), 4000th(d), 5000th(e) iteration are respectively shown.

**Appendix C. Experiment Detail.** In this section we begin to provide some details of our experiments as complementary.

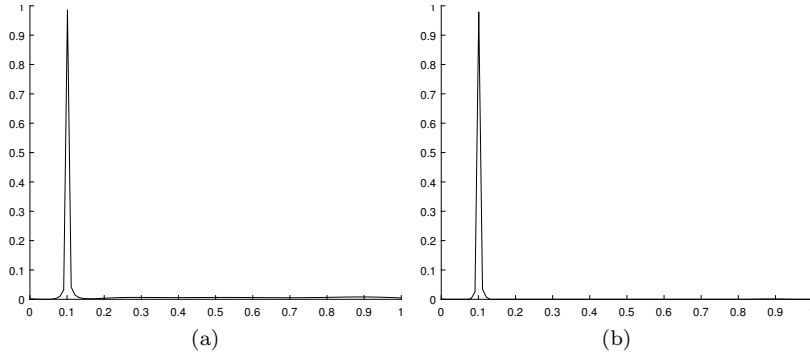


Fig. S3.2: The gap-elimination course for the found spectrum supporting line with series  $y(t) = 100 \sin 20\pi t$ . (a) is the result of source spectrum subtracting found supporting baseline, and one can see that there is some additional noise-gap in the bottom of line subtracted function. (b) is the result after our KDE process to eliminate the gap at the bottom .

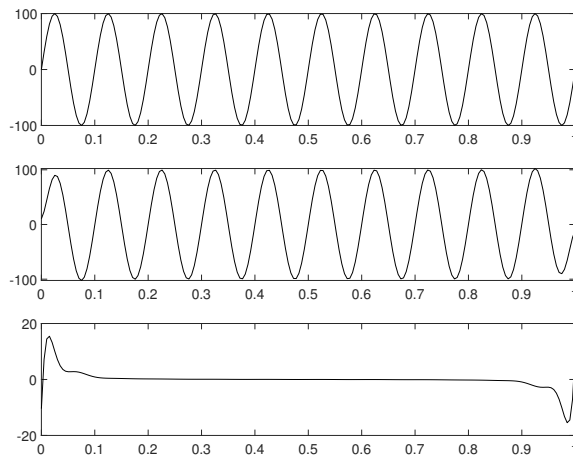


Fig. S3.3: The decomposition result of  $y(t) = 100 \sin 20\pi t$  from the subsequent VMD, using the found number of modes and center frequency as initialization. The subfigure from top to bottom are respective the source signal, the decomposed mode(only one) and the residual.

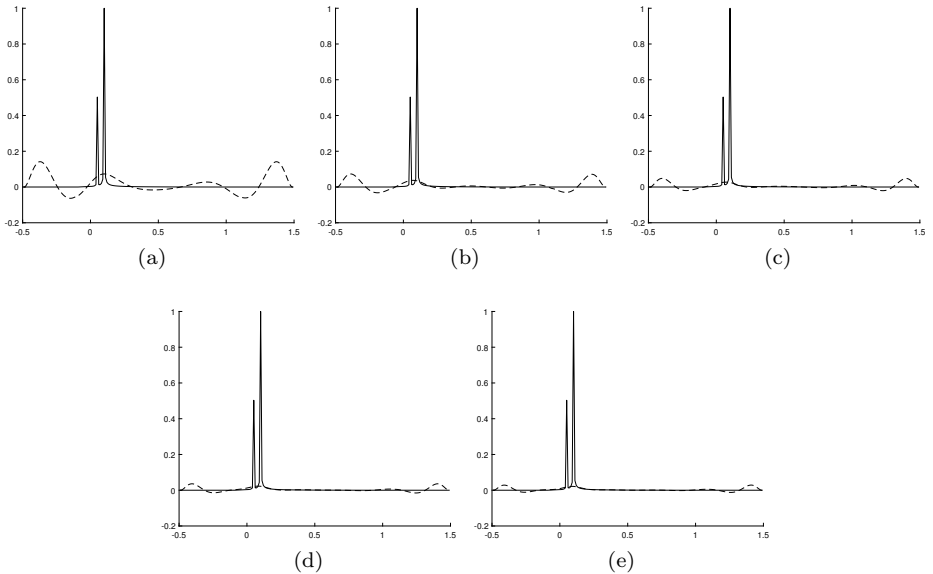


Fig. S3.4: The iteration for finding the supporting baseline of FFT with respect to time series  $y(t) = 10 \cos(10\pi t) + 20 \sin(20\pi t)$ . The 1000th(a), 2000th(b), 3000th(c), 4000th(d), 5000th(e) iterations are respectively shown.

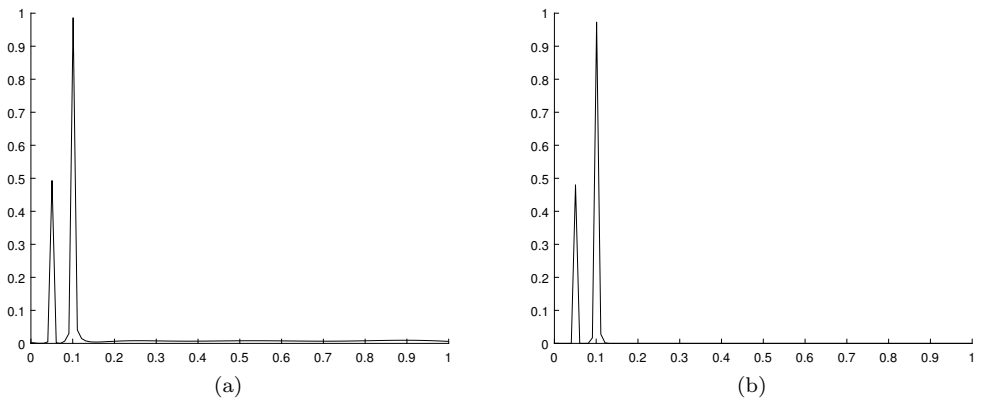


Fig. S3.5: The gap-elimination course for the found spectrum supporting line with series  $y(t) = 10 \cos 10\pi t + 20 \sin 20\pi t$ . (a) is the result of source spectrum subtracting found supporting baseline, and one can see that there is some additional noise-gap in the bottom of line subtracted function. (b) is the result after our KDE process to eliminate the gap at the bottom .

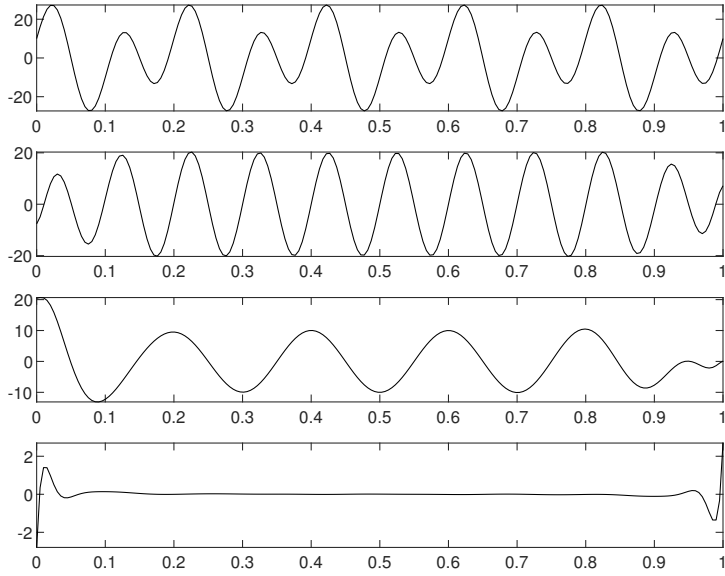


Fig. S3.6: The decomposition result of  $y(t) = 10 \cos 10\pi t + 20 \sin 20\pi t$  from the subsequent VMD, using the found number of modes and center frequency as initialization. The sub-figure from top to bottom are respectively the source signal, the decomposed modes (there are two) and the residual.

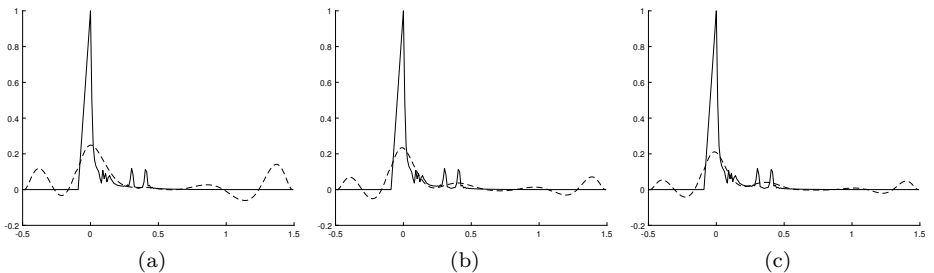


Fig. S3.7: The iteration for finding the supporting baseline of FFT with respect to time series (4.1). The 1000th(a), 2000th(b), 3000th(c) iterations are respectively shown. Note that although the spectrum of second mode,  $\cos 10\pi t$ , is affected by that of the first mode,  $6t^2$ , the computed supporting baseline precisely captured the trend of the lower bound so that all the modes can be filtered out.

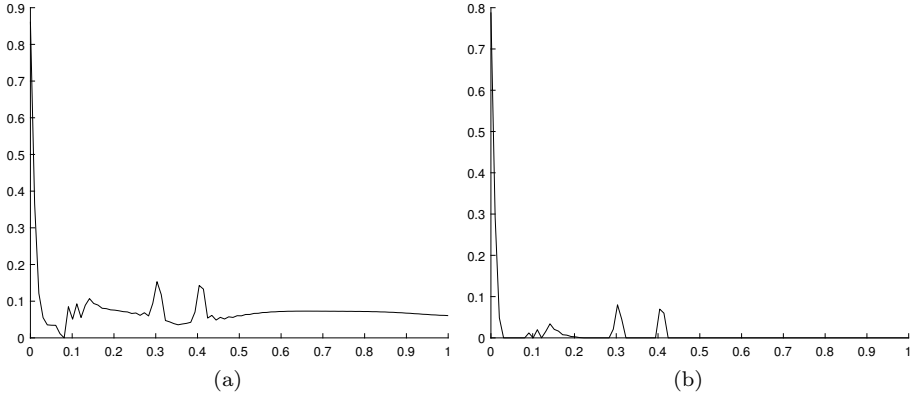


Fig. S3.8: The gap-elimination course for the found spectrum supporting line with series (4.1). (a) is the result of source spectrum subtracting found supporting baseline, and one can see that there is some additional noise-gap in the bottom of line subtracted function. (b) is the result after our KDE process to eliminate the gap at the bottom.

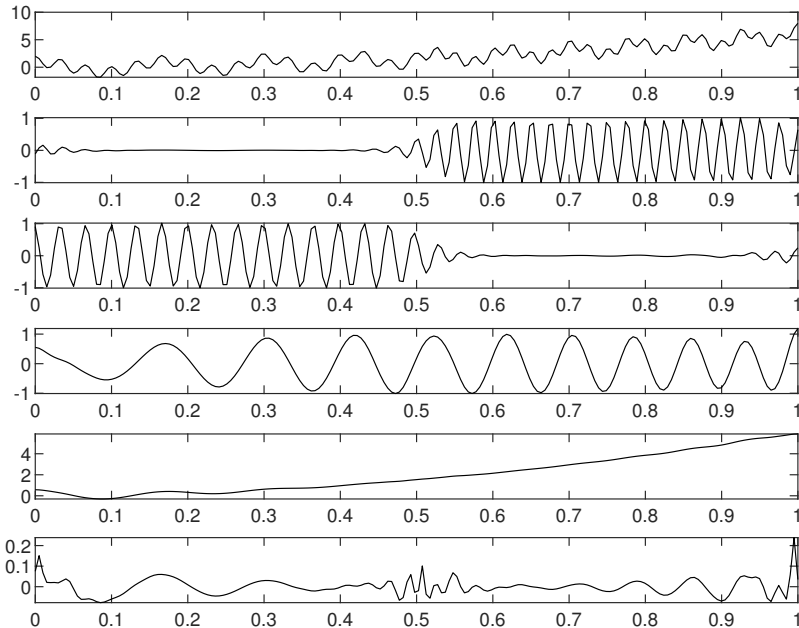


Fig. S3.9: The decomposition result of (4.1) from the subsequent VMD, using the found number of modes and center frequency as initialization. The sub-figure from top to bottom are respectively the source signal, the decomposed modes (there are four) and the residual.

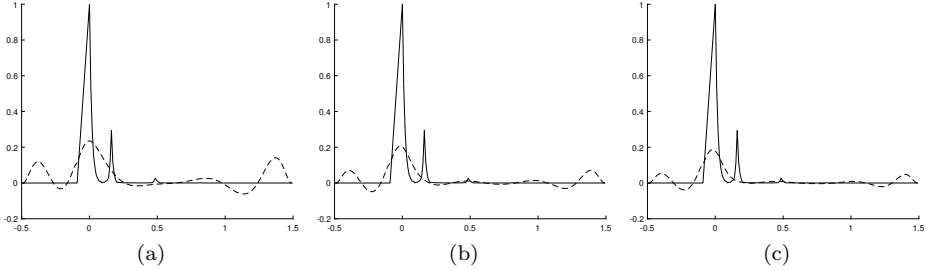


Fig. S3.10: The iterations for finding the supporting baseline of FFT with respect to time series  $\frac{1}{1.2 + \cos 2\pi t} + \frac{\cos(32\pi t + 0.2 \cos 64\pi t)}{1.5 + \sin(2\pi t)}$  are shown. The 1000th(a), 2000th(b), 3000th(c) iterations are respectively shown.

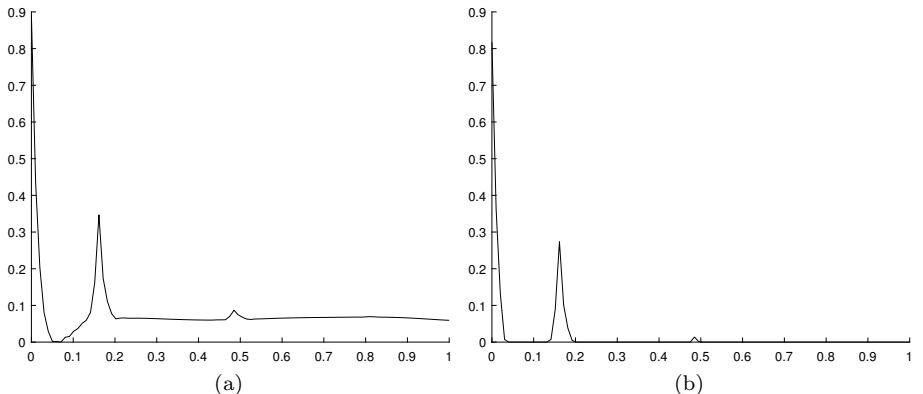


Fig. S3.11: The noise-elimination course for the found spectrum supporting line with series  $\frac{1}{1.2 + \cos 2\pi t} + \frac{\cos(32\pi t + 0.2 \cos 64\pi t)}{1.5 + \sin(2\pi t)}$ . (a) is the result of source spectrum subtracting found supporting baseline, and one can see that there is some additional noise-gap in the bottom of line subtracted function. (b) is the result after our KDE process to eliminate the gap at the bottom .

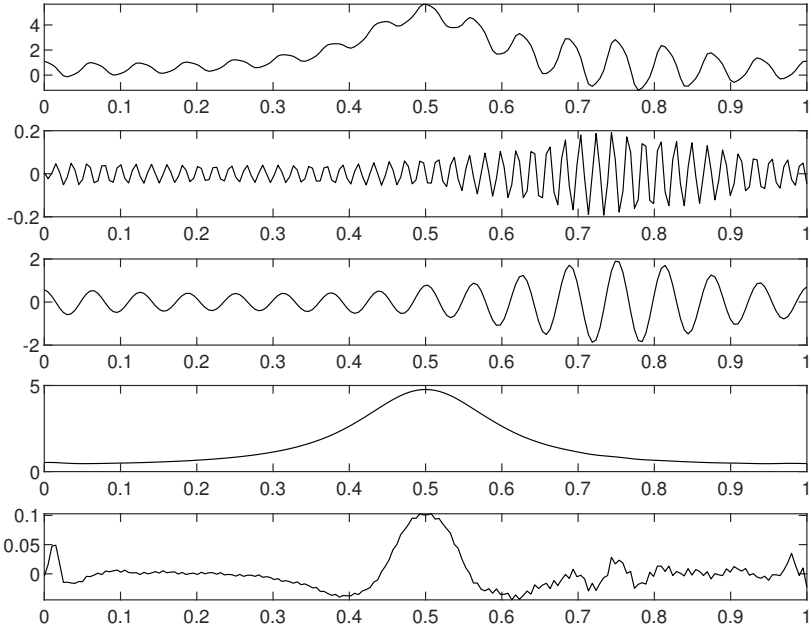


Fig. S3.12: The decomposition result of  $\frac{1}{1.2 + \cos 2\pi t} + \frac{\cos(32\pi t + 0.2 \cos 64\pi t)}{1.5 + \sin(2\pi t)}$  from the subsequent VMD, using the found number of modes and center frequency as initialization.

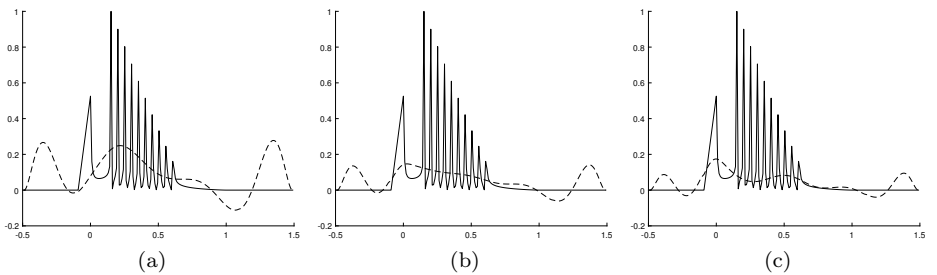


Fig. S3.13: The iteration for finding the baseline of function  $y(t) = 6t + \sum_{i=1}^{10} (13 - i) \cos[(20 + 10i)\pi t]$ , The 500th(a), 1000th(b), 1500th(c) iterations are respectively shown.

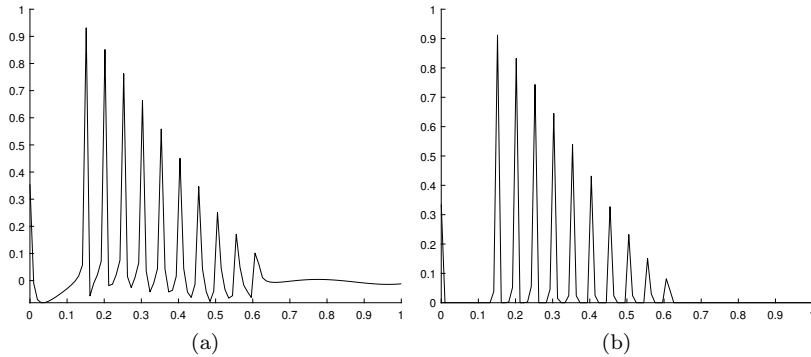


Fig. S3.14: The gap-elimination course for the found spectrum supporting line with series  $y(t) = 6t + \sum_{i=1}^{10} (13 - i) \cos[(20 + 10i)\pi t]$ . (a) is the result of source spectrum subtracting found supporting baseline, and one can see that there is some additional noise-gap in the bottom of line subtracted function. (b) is the result after our KDE process to eliminate the gap at the bottom .

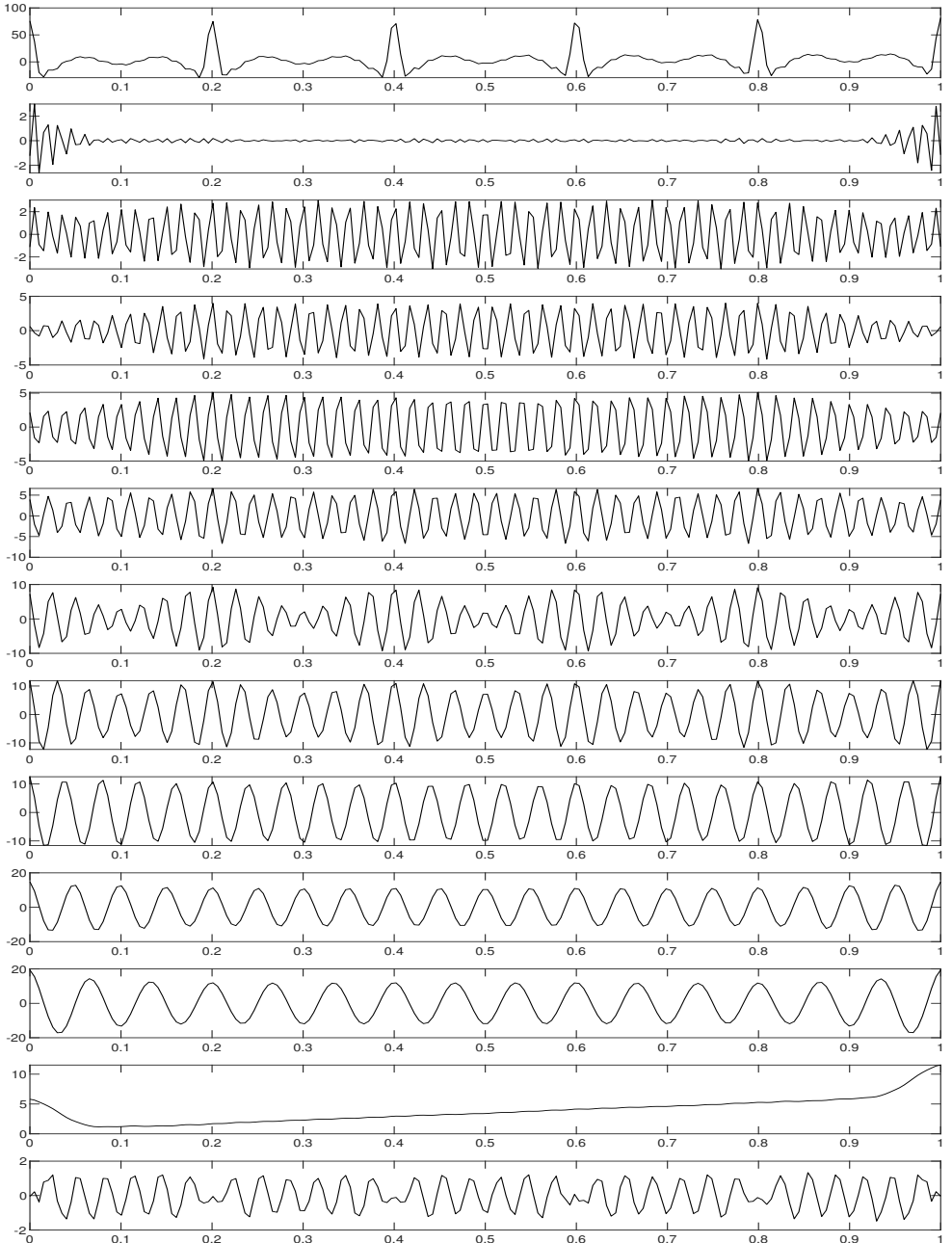


Fig. S3.15: The decomposition result of  $y(t) = 6t + \sum_{i=1}^{10} (13 - i) \cos[(20 + 10i)\pi t]$

from the subsequent VMD, using the found number of modes and center frequency as initialization. The sub-figure from top to bottom are respectively the source signal, the decomposed modes (there are three) and the residual.

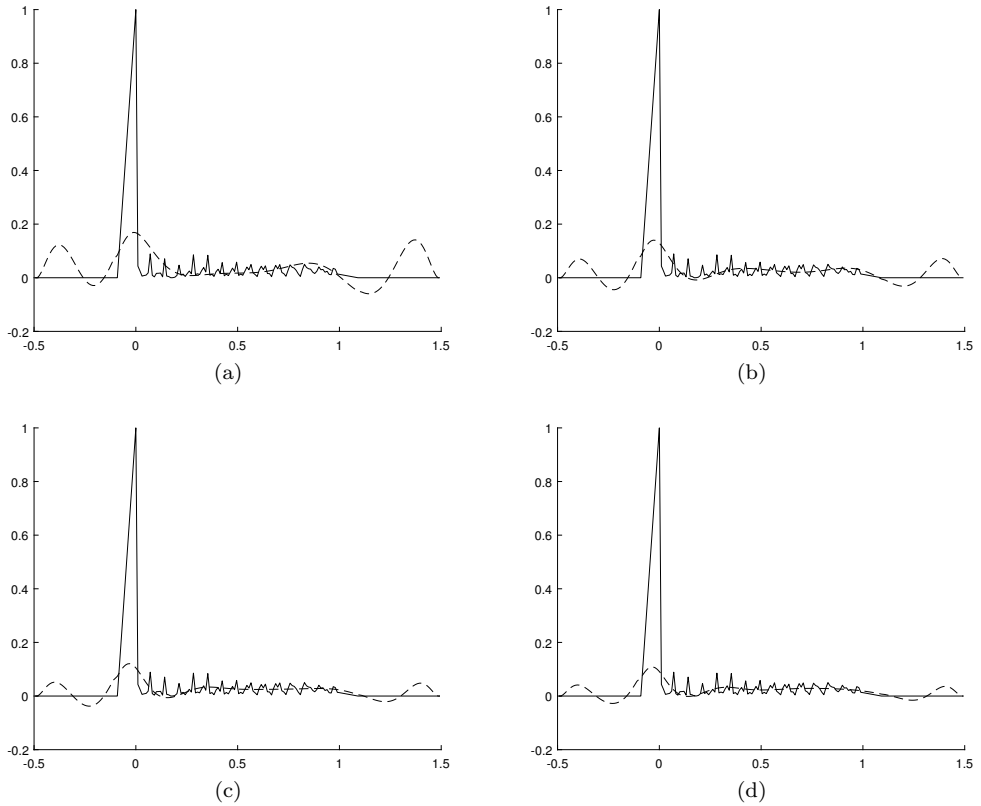


Fig. S3.16: Iterations for finding the supporting baseline without extending the spectrum to MLII lead from record 100 in MIT-BIH Arrhythmia Database. The 1000th(a), 2000th(b), 3000th(c) and 4000th(d) iterations are shown respectively. The solid line are the original spectrum and the dotted line are the evaluated supporting baseline during the iterations. It takes 4140 iterations to achieve the final convergence.

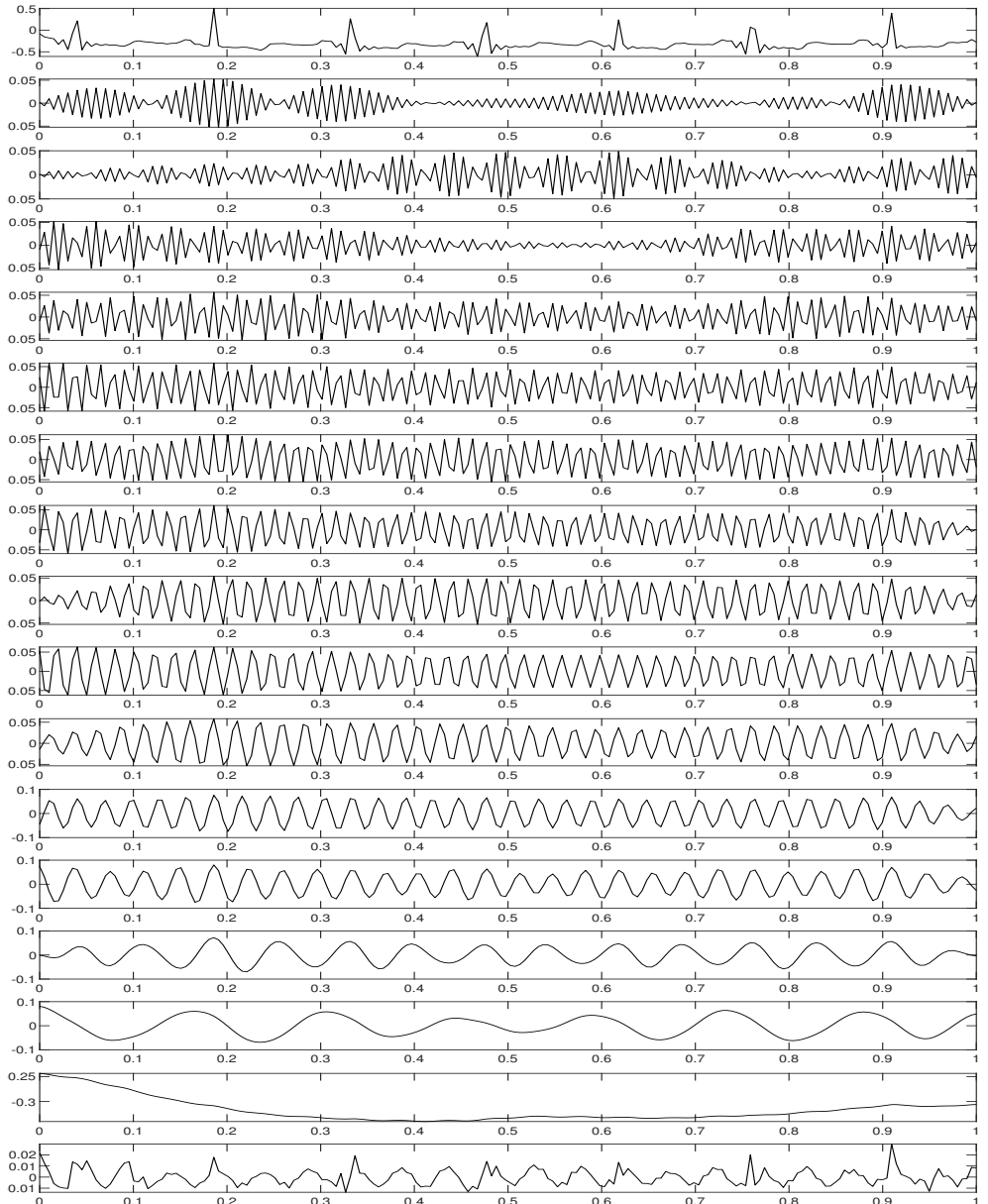


Fig. S3.17: The decomposition result of the MLII lead from record 100 in MIT-BIH Arrhythmia Database. The first line is the original signal and the last the residual, with the 2nd to the 16th lines are the decomposed components acquired by our workflow.

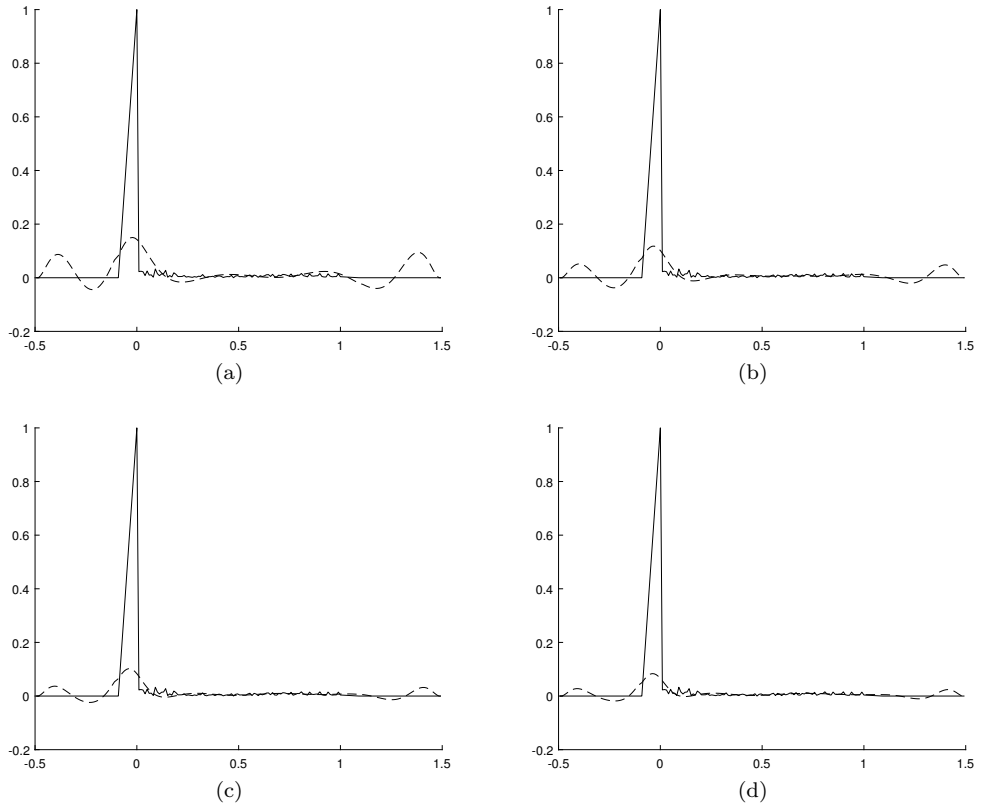


Fig. S3.18: Iterations for finding the supporting baseline without extending the spectrum to V4 lead from record 124 in MIT-BIH Arrhythmia Database. The 1500th(a), 3000th(b), 4500th(c) and 6000th(d) iterations are shown respectively. The solid line are the original spectrum and the dotted line are the evaluated supporting baseline during the iterations. It takes 6899 iterations to achieve the final convergence.

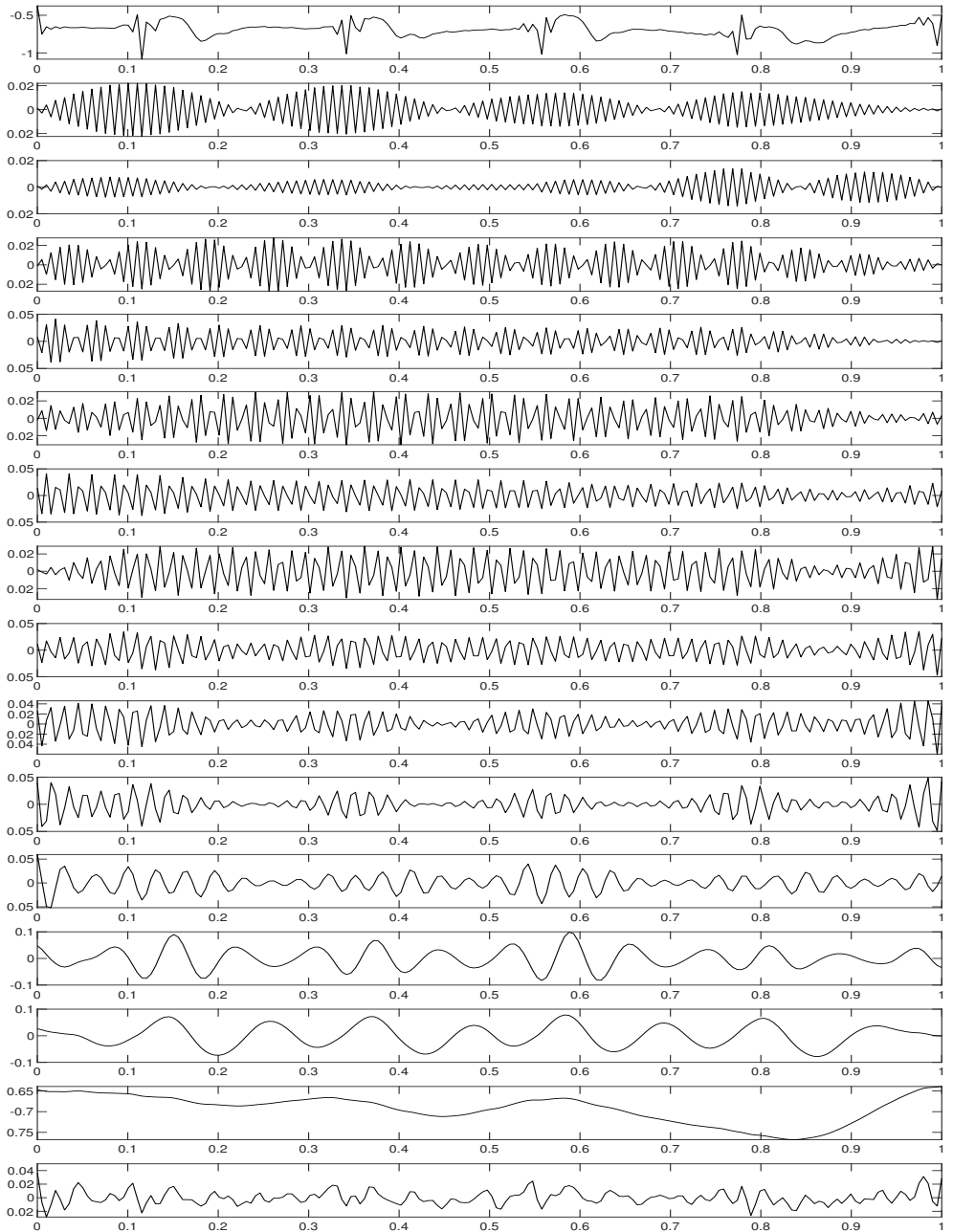


Fig. S3.19: The decomposition result of the V4 lead from record 124 in MIT-BIH Arrhythmia Database. The first line is the original signal and the last the residual, with the 2nd to the 15th lines are the decomposed components acquired by our workflow.